Astronomy & Astrophysics

NIBLES – an H I census of stellar mass selected SDSS galaxies

II. Arecibo follow-up H I observations[⋆]

Z. Butcher[1], S. Schneider[1], W. van Driel[2,3], M. D. Lehnert[4], and R. Minchin[5]

[1] University of Massachusetts, Astronomy Program, LGRT-B 619E, Amherst, MA 01003, USA
   e-mail: zbutcher@astro.umass.edu
[2] GEPI, Observatoire de Paris, CNRS, Université Paris Diderot, 5 place Jules Janssen, 92190 Meudon, France
[3] Station de Radioastronomie de Nançay, Observatoire de Paris, CNRS/INSU USR 704, Université d'Orléans OSUC,
   route de Souesmes, 18330 Nançay, France
[4] Institut d'Astrophysique de Paris, UMR 7095, CNRS, Université Pierre et Marie Curie, 98bis boulevard Arago, 75014 Paris, France
[5] Arecibo Observatory, National Astronomy and Ionosphere Center, Arecibo, PR 00612, USA

ABSTRACT

We obtained Arecibo H I line follow-up observations of 154 of the 2600 galaxies in the Nançay Interstellar Baryons Legacy Extragalactic Survey (NIBLES) sample. These observations are on average four times more sensitive than the original observations at the Nançay Radio Telescope. The main goal of this survey is to characterize the underlying H I properties of the NIBLES galaxies which were undetected or marginally detected at Nançay. Of the Nançay non-detections, 85% were either clearly or marginally detected at Arecibo, while 89% of the Nançay marginal detections were clearly detected. Based on the statistics of the detections relative to $g - i$ color and r-band luminosity (L_r) distribution among our Arecibo observations, we anticipate ~60% of our 867 Nançay non-detections and marginal detections could be detected at the sensitivity of our Arecibo observations. Follow-up observations of our low luminosity ($L_r < 10^{8.5}$ $L_\odot$) blue sources indicate that they have, on average, more concentrated stellar mass distributions than the Nançay detections in the same luminosity range, suggesting we may be probing galaxies with intrinsically different properties. These follow-up observations enable us to probe H I mass fractions, $\log(M_{HI}/M_\star)$ 0.5 dex and 1 dex lower, on average, than the NIBLES and ALFALFA surveys respectively.

Key words. surveys – galaxies: general – galaxies: distances and redshifts – radio lines: galaxies – galaxies: ISM

1. Introduction

The optical luminosity function (LF) and the H I mass function (HIMF) are two of the most important and fundamental tracers of the volume density distribution of galaxies in the universe. They yield clues to both the baryonic and dark matter content of galaxies, as well as their evolutionary histories. Consequently, there are many applications for which the LF and HIMF can be used, for example, as constraints in galaxy formation models (see, e.g., Benson et al. 2003; Lu et al. 2014).

Many studies have attempted to constrain both of these functions over the years. Since the LF was first fitted to an analytic form by Schechter (1976), many subsequent studies have attempted to analyze its various properties and constrain its parameters (see, e.g., Felten 1985; Efstathiou et al. 1988; Loveday et al. 1992, 2015; Blanton & Collaboration 2001; Blanton et al. 2003; Montero-Dorta & Prada 2009; McNaught-Roberts et al. 2014). The HIMF, having the same functional form as the LF, has also been analyzed in detail, although to a somewhat lesser extent (see, e.g., Zwaan et al. 1997, 2003; Kilborn et al. 1999; Kovac et al. 2005; Springob et al. 2005; Martin et al. 2010; Hoppmann et al. 2015).

To date, both these functions have been treated separately in their analyses. One of the main goals of the Nançay Interstellar Baryons Legacy Extragalactic Survey (NIBLES) is to study the inter-relation between these two fundamental population tracers. More specifically, we want to analyze the HIMF and other galaxy properties as a function of optical luminosity. To achieve this goal, we carried out a 21 cm H I line survey at the 100 m class Nançay Radio Telescope (NRT). The final observed sample consists of 2600 galaxies selected from the Sloan Digital Sky Survey (SDSS; see, e.g., York et al. 2000) with radial velocities $900 < cz < 12\,000$ km s^{-1}. The galaxies were selected to be distributed evenly over their entire range of absolute z-band magnitudes (~−13.5 to −24), which was used as a proxy for total stellar mass – see van Driel et al. (2016, Paper I) for further details.

The NIBLES galaxy selection criteria are:

1. must have both SDSS magnitudes and optical spectrum;
2. must lie within the local volume ($900 < cz < 12\,000$ km s^{-1});
3. uniform sampling of each 0.5 mag wide bin in absolute z-band magnitude, M_z;
4. preferentially observe nearby objects;
5. no a priori selection on color.

NIBLES, with its relatively uniform selection of galaxies that are based on total stellar mass, is aimed to complement other recent and/or ongoing large H I surveys in the local volume, in particular, blind surveys such as ALFALFA (e.g., Haynes et al. 2011).

[⋆] Reduced spectra are only available at the CDS via anonymous ftp to cdsarc.u-strasbg.fr (130.79.128.5) or via http://cdsarc.u-strasbg.fr/viz-bin/qcat?J/A+A/596/A60

One main advantage of NIBLES over blind H I surveys is our increased on-source integration time, which enables us to reduce the rms noise of the observations. Each NIBLES source was initially observed at Nançay for about 40 min of telescope time, resulting in a mean rms noise of ~3 mJy at 18 km s^{-1} resolution. In the case of weak or non-detections, observations were repeated (as time allowed) resulting in a target rms noise between 1.5 and 1.8 mJy for the majority of our undetected sample. However, there were a number of sources where follow-up time was unavailable to achieve the desired rms, which resulted in a mean of 2.3 mJy for the remainder of the undetected sample, yielding a bimodal rms noise distribution (see Paper I).

Of the 2600 NIBLES galaxies, 1733 (67%) were clearly detected, 174 (7%) marginally detected, and 693 (27%) were not detected. To adequately quantify our H I distribution across the optical LF, we need to gain a statistical understanding of the underlying H I distribution of sources which were undetected at Nançay. We therefore carried out pointed observations of 90 undetected or marginally detected galaxies at the 305 m Arecibo radio telescope, which gives us a noise level reduction by about a factor of four. Additionally, we had a number of sources suffering from observational problems at Nançay which we reobserved at Arecibo, and during periods of time when primary target sources were unavailable, we observed detected NIBLES sources to compare flux calibrations at the two observatories. In total, we observed 154 galaxies from the NIBLES sample (see Sect. 2 and Paper I for details).

Here we present the results from these follow-up observations along with a brief synopsis of the differences in the data between the Nançay and Arecibo samples. The main purpose of this paper is data presentation. Further analysis will be carried out in subsequent papers. In Sect. 2 we describe the selection of the observed sample of galaxies and in Sect. 3, the observations and data reduction. The results are presented in Sect. 4 and discussed in Sect. 5 We present our conclusions in Sect. 6. An analysis of this data regarding the impact on our H I distribution as a function of optical luminosity will be presented in Paper III (Butcher et al., in prep.). All source numbers presented in this paper refer to the NIBLES source number, which can be cross-referenced with other common source names in the tables presented here and in Paper I.

2. Sample selection

Our total sample of Arecibo follow-up galaxies consists of 154 sources. Of these, 90 are classified as either non-detections or marginal detections at Nançay, with the remaining 64 consisting of sources initially suffering from observational problems such as OFF beam detections or RFI and a handful of sources used for flux comparison between the two telescopes. Of these 64, ten were excluded from the original NIBLES catalog because their Nançay observations contained technical problems which we were not able to overcome (listed in Table 5).

Of the 90 Nançay non-detected or marginally detected galaxies, 59 were selected based on color ($u-z < 2$) and radial velocity ($cz < 4000$ km s^{-1}) for the specific reason that these blue, nearby galaxies would normally be expected to have H I and yet were undetected at Nançay.

3. Observations and data reduction

The Arecibo radio telescope uses a 305 m diameter spherical primary mirror and covers a declination range of $-1° < \delta < 38°$ with pointing accuracy of about 5″. We used the L-band

wideband receiver (L-wide) with the Wideband Arecibo Pulsar Processor (WAPP) correlator backend using two polarizations with a bandpass of 50 MHz (approximately 10 600 km s^{-1}) across 4096 frequency channels corresponding to a channel separation of 2.6 km s^{-1} at $z \sim 0$. The L-wide receiver has a half power beam width of approximately 3′.5 and yields an effective system temperature typically between 28 and 32 K. Data were taken in standard 5/5 min integration ON/OFF position switching mode. All galaxies were observed for a minimum of one 5/5 min cycle, and some of the blue low-luminosity galaxies were observed longer depending on telescope time and signal strength after the first observation.

Throughout this paper, all radial velocities given are heliocentric, and all H I-line related parameters are according to the conventional optical definition ($V = c(\lambda - \lambda_0)/\lambda_0$).

Observations were carried out in two sessions, between December 2008 and October 2009 and between March and September 2012 for a total of 59 h.

Data were reduced using a combination of Phil Perillat's IDL routines and Robert Minchin's CORMEASURE routine from the Arecibo Observatory. All H I spectra were Hanning smoothed to a median velocity resolution of 18.7 km s^{-1} to match the 18 km s^{-1} resolution of the NRT spectra as closely as possible. All H I spectra shown here have a heliocentric, optical (cz) radial velocity scale.

Two of our sources, 1260 and 2434 (i.e., PGC 4546173 and CGCG 427-032), suffered from a baseline ripple with a wavelength corresponding to approximately 210 km s^{-1} which we were able to remove via a Fourier transform, see Appendix A for details.

4. Results

The Arecibo observations enabled us to probe our sample about four times deeper on average than at Nançay. The mean rms noise of the Nançay undetected sample is 2.33 mJy whereas the mean rms noise of our Arecibo observations is 0.57 mJy, both at 18 km s^{-1} resolution.

As with our Nançay data, we divided the sources into detected, marginally detected, and non-detected categories. This was accomplished through visual inspection of each H I spectrum by three independent adjudicators (ZB, WvD, SES). Disagreements were discussed until a consensus was reached. The galaxies in the marginal detection category have H I line spectra with a peak signal-to-noise ratio less than four, but coinciding with the SDSS optical velocity. The galaxies in this category would most likely be missed in a survey of objects with previously unknown velocity. However, the low probability of a strong noise peak coinciding with the SDSS optical velocity lends greater credibility to the likelihood that these peaks represent real signals.

There is generally very good agreement (<3 km s^{-1} on average) between the DR9 heliocentric velocities and our H I velocities, with the exception of three cases. These three outliers, sources 1631, 2434, and 2606 (i.e., NGC 4290, CGCG 427-032, and NGC 3772 respectively) all have velocity discrepancies larger than 50 km s^{-1}. Source 1631 has the SDSS spectral fiber positioned out in its disk, blueshifting the overall redshift measurement. Source 2434 is confused with a secondary source in the Arecibo beam, but source 2606 suffers no obvious signs of confusion or spectral fiber offsets and the optical spectrum does not appear noisy (see Fig. B.1). However, source 2606 is also listed in de Vaucouleurs et al. (1991) as having a heliocentric

velocity of 3478 ± 50 km s^{-1} which agrees with our H I velocity of 3423 ± 7 km s^{-1}.

The optical data listed are in general from the SDSS DR9 (see also Paper I) with the median total stellar masses and star-formation rates taken from the corresponding publicly available SDSS added-value MPA-JHU catalogs (Brinchmann et al. 2004; Kauffmann et al. 2003; Salim et al. 2007; Tremonti et al. 2004) where available. In cases where estimates are not available, stellar masses, specific star formation rates (sSFR), and gas mass fractions ($\log(M_{HI}/M_\star)$) are marked as "—".

Due to the limited redshift range of NIBLES, the difference in luminosity distances used for our H I masses and the stellar mass estimates from MPA-JHU are less than a few percent in the most extreme cases. This systematic difference is far less than the typical uncertainty in the stellar mass estimates themselves, which are on the order of 20%.

Listed throughout the tables are the following properties of the target galaxies:

– RA and Dec: Right Ascension and Declination in J2000.0 coordinates, as used for the observations;
– other name: common catalog name, other than the SDSS;
– V_{opt}: heliocentric radial velocity (cz) measured in the optical (in km s^{-1}), from Paper I;
– $\log(M_\star)$: total median stellar mass estimates (in $M_\odot$);
– $\log(sSFR)$: specific star formation rate, or $SFR/M_\star$ (in yr^{-1});
– $g - z$: $g - z$ integrated color of the galaxy using SDSS model magnitudes, corrected for Galactic extinction, following Schlegel et al. (1998; in mag);
– M_g: integrated absolute g-band model magnitude, corrected for Galactic extinction following Schlegel et al. (1998);
– rms: rms noise level values of the H I spectra (in mJy);
– V_{HI}: heliocentric radial velocity (cz) of the center of the H I line profile (in km s^{-1});
– W_{50}, W_{20}: velocity widths measured at 50% and 20% of the H I profile peak level, respectively, uncorrected for galaxy inclination (in km s^{-1});
– F_{HI}: integrated H I line flux (in Jy km s^{-1});
– SNR: peak signal-to-noise ratio, which we define as the peak flux density divided by the rms; For non-detections, the SNR listed is the maximum found in the expected velocity range of the H I profile;
– S/N: signal-to-noise ratio determined taking into account the line width, following the ALFALFA H I survey formulation from Saintonge (2007): $S/N = 1000(F_{HI}/W_{50})(W_{50}/2R)^{0.5}$/rms, where R is the velocity resolution, 18.7 km s^{-1} on average;
– $\log(M_{HI})$: total H I mass (in $M_\odot$), where $M_{HI} = 2.36 \cdot 10^5 \cdot D^2.F_{HI}$, where $D = V/70$ is the galaxy's distance (in Mpc). In the cases of non-detections, 3σ upper limits are listed for a flat-topped profile with a width depending on the target's r-band luminosity, L_r, according to the upper envelope in the $W_{20} - L_r$ relationship of our Nançay clear, non-confused detections (see Paper I);
– $\log(M_{HI}/M_\star)$: ratio of the total H I and stellar masses.

Estimated uncertainties are given after the values in the tables. Uncertainties in the central H I line velocity, V_{HI}, and in the integrated H I line flux, F_{HI}, were determined following Schneider et al. (1986, 1990) as, respectively

$$\sigma_{V_{HI}} = 1.5(W_{20} - W_{50})SNR^{-1} \text{ (km s}^{-1}) \tag{1}$$

$$\sigma_{F_{HI}} = 2(1.2W_{20}R)^{0.5}\text{rms (km s}^{-1}) \tag{2}$$

where R is the instrumental resolution, 18.7 km s^{-1}, SNR is the peak signal-to-noise ratio of a spectrum and rms is the root mean square noise level (in Jy). Following Schneider et al., the uncertainty in the W_{50} and W_{20} line widths is expected to be 2 and 3.1 times the uncertainty in V_{HI}, respectively.

Table 1 lists all 72 sources detected at Arecibo which were either undetected (55 sources) or marginally detected (17 sources) at Nançay. Table 2 lists the five Arecibo marginal detections which were undetected at Nançay, and Table 3 lists the 15 sources not detected at Arecibo, including 11 Nançay non-detections, two Nançay marginal detections and two others flagged as NRT confused detections which were not detected at Arecibo due to its smaller beam size.

In Table 4 we compare line flux parameters of galaxies we detected at both Arecibo and Nançay and in Table 5 we list the ten sources detected at Arecibo which were not included in our final Nançay sample due to data problems (see Paper I).

The following types of cases have been flagged in the tables following the naming conventions in Paper I:

– C (3 cases): H I detection of the target galaxy confused by another galaxy within the Arecibo telescope beam;
– C3 (1 case): H I detection of the target galaxy confused by another galaxy in the Arecibo telescope beam, but the secondary source likely contributes a minor amount of flux to the total observed flux;
– K (8 cases): Nançay H I detection either clearly or possibly confused by another galaxy within the NRT beam;
– D (2 cases): baseline ripple removed from H I spectrum (see Sect. 3);
– M (19 cases): original Nançay detection classification changed to marginally detected;
– R (2 cases): sources possibly resolved by the Arecibo beam. These sources have an SDSS optical image with a diameter about the same size as the Arecibo beam which is expected to lead to an underestimate of their total H I flux.

Color SDSS images alongside the H I line spectra of our Arecibo detections are shown in Fig. B.1, marginal detections are presented in Fig. B.2, and non-detections in Fig. B.3.

Due to the updated detection category classifications and reprocessing of the Nançay data, our Arecibo follow-up sample now consists of 54 galaxies detected at Nançay (of which 52 were detected at Arecibo and the remaining two are confused detections at Nançay where the signal is from a secondary source) as well as 90 galaxies which are either undetected (71) or marginally detected (19) at Nançay and ten galaxies for which we have no useable Nançay data. These ten have been added to the NIBLES catalog and assigned succeeding source numbers, see Table 5.

4.1. Flux comparison between Arecibo and Nançay

For our ten calibration sources which have a Nançay peak signal-to-noise ratio greater than 8, we compared the H I line flux ratios at both telescopes using a weighted mean. Each source was weighted by the inverse square of its flux uncertainty to more heavily weight the sources with lower errors. The resulting Arecibo/NRT flux ratio is 1.19 ± 0.08 where the uncertainty is given by the standard deviation of the weighted mean. This offset is consistent with the flux offset discussed in Paper I, however detailed analysis of this flux scale difference is beyond the scope of this paper (see Paper I for details).

Table 1. Basic optical and HI data – Arecibo detections of Nançay non-detections and marginals.

| Source	RA	Dec (J2000.0)	Name	V_{opt} km s^{-1}	$g-z$ mag	M_g mag	$M_\star$ [log] $M_\odot$	sSFR [log] yr^{-1}	rms mJy	V_{HI} km s^{-1}	W_{50} km s^{-1}	W_{20} km s^{-1}	F_{HI} Jy km s^{-1}	SNR	S/N	M_{HI} [log] $M_\odot$	$M_{HI}/M_\star$ [log]
0023	00 10 25.50	14 17 23.00	KUG 0007+140	5452 ± 4	0.93	-18.81	9.50	-10.17	0.45	5456 ± 3	189	208	0.60 ± 0.06	8.4	15.4	8.93	-0.57
0037^M	00 15 05.40	15 03 59.70	2MASX J00150533+1503597	5428 ± 2	1.37	-19.15	10.00	-10.55	0.53	5436 ± 20	81	164	0.30 ± 0.07	6.0	10.2	8.63	-1.37
0038	00 15 29.70	14 43 37.20	ASK 147494	5432 ± 3	0.39	-16.55	8.21	-9.54	0.17	5445 ± 3	65	76	0.04 ± 0.01	4.9	4.7	7.77	-0.44
0297	02 00 03.80	14 07 12.90	ASK 43581	4860 ± 2	0.39	-16.52	6.14	-8.70	0.57	4860 ± 2	120	139	0.66 ± 0.06	10.8	16.9	8.87	2.73
0329^M	02 50 52.00	00 00 12.10	ASK 037212	1587 ± 2	0.24	-14.16	7.19	-9.59	0.17	1579 ± 1	26	41	0.07 ± 0.01	12.2	12.4	6.91	-0.27
0340	03 01 11.90	00 18 10.50	PGC 1162351	2779 ± 2	0.61	-15.67	7.94	-9.52	0.54	2793 ± 10	34	92	0.21 ± 0.05	8.0	10.7	7.90	-0.05
0349^M	03 07 15.65	00 43 52.00	ASK 37834	3011 ± 1	0.47	-15.60	7.74	-9.43	0.58	3030 ± 3	79	100	0.49 ± 0.06	10.2	15.4	8.33	0.59
0475	07 35 24.20	36 38 36.40	ASK 44962	3902 ± 1	0.42	-16.86	8.23	-9.48	0.81	3887 ± 8	86	141	0.79 ± 0.09	9.9	17.1	8.76	0.53
0562	07 59 16.20	23 50 58.10	ASK 265000	2231 ± 2	0.69	-14.88	7.73	-9.96	0.40	2242 ± 7	49	72	0.08 ± 0.03	4.5	4.4	7.26	-0.47
0575	08 01 32.20	21 22 47.80	ASK 363277	2104 ± 3	0.56	-15.63	7.86	-9.52	0.50	2103 ± 3	47	78	0.46 ± 0.04	13.6	21.8	7.99	0.13
0602	08 15 38.03	21 15 37.20	ASK 483519	3476 ± 1	0.45	-16.28	7.94	-9.31	0.51	3487 ± 12	56	140	0.45 ± 0.06	9.8	19.1	8.42	0.48
0609	08 17 21.00	24 57 45.60	KUG 0814+251	2074 ± 4	0.61	-15.55	7.91	-9.58	0.36	2062 ± 7	88	131	0.29 ± 0.04	8.4	14.0	7.77	-0.13
0645	08 23 41.00	20 41 48.50	ASK 522849	2011 ± 10	0.67	-14.19	7.49	-9.75	0.45	2024 ± 8	43	70	0.10 ± 0.04	5.0	5.3	7.28	-0.21
0689	08 36 41.10	05 16 24.00	ASK 259050	3127 ± 1	0.20	-15.72	7.54	-8.93	0.46	3126 ± 5	55	90	0.28 ± 0.04	9.5	13.3	8.12	0.58
0708^M	08 42 25.80	06 35 38.60	ASK 259104	2260 ± 1	0.33	-15.48	7.60	-9.28	0.54	2254 ± 4	50	85	0.47 ± 0.05	12.4	19.8	8.06	0.46
0719	08 44 42.70	29 32 43.00	ASK 281794	2116 ± 2	0.40	-14.49	7.26	-9.29	0.50	2135 ± 8	69	109	0.21 ± 0.05	7.0	8.2	7.66	0.40
0724	08 45 25.40	15 19 46.00	PGC 4176159	1614 ± 8	0.02	-13.43	7.30	-10.72	0.36	1598 ± 7	35	72	0.10 ± 0.03	7.0	7.9	7.11	-0.19
0751	08 50 25.19	32 37 18.80	ASK 266943	2221 ± 1	0.56	-14.82	7.21	-9.37	0.52	2219 ± 5	44	63	0.10 ± 0.04	4.9	4.9	7.39	0.18
0801^M	09 08 52.55	21 55 29.70	2MASX J09085253+2155292	3849 ± 1	0.66	-17.03	8.51	-9.63	0.59	3851 ± 3	51	77	0.36 ± 0.05	10.0	13.8	8.41	-0.10
0828	09 14 57.30	06 00 18.60	ASK 261057	1370 ± 29	0.64	-14.37	–	–	0.32	1370 ± 8	28	54	0.04 ± 0.02	4.6	4.3	6.60	–
0850^M	09 20 02.70	28 20 57.40	ASK 488350	1915 ± 7	0.52	-14.23	7.35	-9.55	0.49	1920 ± 3	63	83	0.29 ± 0.04	8.6	11.9	7.70	0.35
0904	09 40 45.80	32 28 20.80	KUG 0937+327	1293 ± 1	0.44	-14.20	7.13	-9.32	0.51	1280 ± 11	54	103	0.19 ± 0.05	6.2	8.5	7.19	0.06
0928	09 46 53.00	31 47 44.60	KUG 0943+320	1425 ± 3	0.64	-14.40	7.47	-9.70	0.47	1424 ± 5	59	92	0.27 ± 0.04	8.4	12.3	7.43	-0.04
0938^M	09 48 47.50	27 52 25.40	ASK 491818	1316 ± 1	0.51	-14.56	7.30	-9.37	0.85	1318 ± 10	34	73	0.20 ± 0.07	5.5	6.6	7.22	-0.07
0949	09 52 35.10	08 11 56.60	ASK 277328	2725 ± 3	0.72	-16.92	8.53	-9.75	0.56	2723 ± 2	105	120	0.53 ± 0.06	9.3	15.1	8.28	-0.25
0952^M	09 54 30.00	32 03 42.00	ASK 492645	1424 ± 2	0.40	-13.50	7.01	-9.47	0.66	1434 ± 2	87	101	0.49 ± 0.06	8.4	13.2	7.69	0.68
0976	10 01 09.50	08 46 55.50	ASK 277703	1265 ± 2	0.63	-13.67	7.14	-9.61	0.62	1260 ± 2	28	39	0.13 ± 0.04	7.0	6.5	7.00	-0.14
0987^M	10 04 25.10	02 33 31.00	ASK 68781	1125 ± 2	-0.38	-11.91	7.12	-9.59	0.55	1131 ± 2	32	53	0.33 ± 0.04	12.5	17.2	7.30	0.19
0991^M	10 06 10.80	11 06 02.10	ASK 295498	2499 ± 1	0.48	-16.95	6.10	-8.41	0.62	2509 ± 3	101	123	0.58 ± 0.07	9.1	15.2	8.24	2.15
1017	10 16 59.00	03 42 35.40	ASK 95821	1204 ± 1	0.63	-14.10	–	–	0.58	1212 ± 3	29	46	0.17 ± 0.04	8.2	8.7	7.07	–
1030	10 19 59.90	24 47 24.60	ASK 596355	1258 ± 1	0.42	-14.06	7.08	-9.48	0.63	1256 ± 4	35	56	0.17 ± 0.04	7.4	7.3	7.10	0.02
1069	10 35 11.10	25 27 04.00	PGC 4243890	1298 ± 1	0.24	-13.32	6.62	-8.98	0.53	1297 ± 4	34	56	0.16 ± 0.04	7.4	8.4	7.11	0.49
1095	10 44 20.70	14 05 04.00	NGC 3357	9770 ± 2	1.51	-22.32	11.41	-12.52	0.77	9740 ± 11	113	152	0.39 ± 0.09	5.2	7.6	9.25	-2.16
1147	11 00 47.10	16 52 55.50	PGC 4260762	1136 ± 1	0.51	-13.25	6.93	-9.56	1.06	1132 ± 5	41	59	0.21 ± 0.08	4.9	5.1	7.12	0.19
1166	11 07 09.90	28 22 31.90	PGC 1833985	1003 ± 1	0.42	-13.87	7.09	-9.49	0.48	1006 ± 4	42	79	0.34 ± 0.04	11.8	18.0	7.22	0.13
1260^D	11 25 04.00	28 09 35.60	PGC 4546173	1593 ± 1	-0.01	-14.24	6.76	-8.80	0.85	1580 ± 9	38	65	0.16 ± 0.07	4.2	4.8	7.27	0.51
1388	11 47 06.90	03 06 23.00	ASK 74477	1016 ± 2	0.44	-13.16	6.71	-9.29	0.19	1021 ± 2	31	53	0.09 ± 0.01	11.0	13.1	6.64	-0.08
1419	11 52 24.06	32 24 13.90	NGC 3935	3066 ± 2	1.37	-19.60	10.22	-10.77	0.51	3075 ± 19	78	152	0.27 ± 0.06	5.7	9.9	8.09	-2.12
1424	11 53 00.30	16 02 29.40	ASK 436517	905 ± 29	0.63	-12.08	–	–	0.58	931 ± 4	27	42	0.09 ± 0.04	4.6	5.0	6.59	–
1453	11 57 25.10	02 11 15.90	PGC 1218832	1019 ± 1	0.49	-13.16	6.80	-9.49	0.62	1019 ± 1	35	56	0.22 ± 0.04	8.9	9.7	7.04	0.24
1751^M	12 54 12.60	00 48 09.10	CGCG 015-035	1191 ± 1	0.64	-15.29	–	–	0.65	1197 ± 2	61	81	0.62 ± 0.06	12.6	20.0	7.63	–
1807	13 09 36.90	31 40 34.00	PGC 1958740	2159 ± 4	-0.05	-15.06	7.56	-9.91	0.25	2156 ± 4	41	79	0.24 ± 0.02	14.1	24.7	7.73	0.17
1877	13 34 06.90	09 15 43.20	PGC 454337	1112 ± 11	0.51	-13.70	7.30	-10.09	0.26	1134 ± 2	26	39	0.07 ± 0.02	8.8	8.1	6.62	-0.69

Notes. Marginal Nançay detections are flagged with an M and sources affected by the baseline ripple with a D. For a description of other flags, see Sect. 4.

Table 1. continued.

Source	RA	Dec (J2000.0)	Name	V_{opt} km s^{-1}	$g - z$ mag	M_g mag	$M_\star$ [log] $M_\odot$	sSFR [log] yr^{-1}	rms mJy	V_{HI} km s^{-1}	W_{50} km s^{-1}	W_{20} km s^{-1}	F_{HI} Jy km s^{-1}	SNR	S/N	M_{HI} [log] $M_\odot$	$M_{HI}/M_\star$ [log]
1879	13 35 37.20	14 21 39.40	PGC 1456087	993 ± 21	0.78	−13.81	–	–	0.45	1040 ± 7	27	49	0.06 ± 0.03	4.6	4.0	6.48	–
1987^M	13 57 21.10	26 12 27.20	PGC 1767195	2391 ± 4	0.57	−14.70	7.52	−9.55	0.32	2360 ± 6	38	72	0.12 ± 0.03	8.1	10.1	7.51	−0.01
1988	13 57 23.60	05 34 25.20	ASK 179268	994 ± 20	0.35	−14.95	–	–	0.36	1008 ± 1	42	55	0.17 ± 0.03	10.3	11.9	6.93	–
1998	13 58 45.00	24 09 05.00	2MASX J13584501+2409048	970 ± 2	0.76	−13.86	7.34	−9.86	0.37	984 ± 2	63	82	0.30 ± 0.03	11.2	16.5	7.14	−0.19
2084	14 17 07.50	04 50 13.40	ASK 99987	1643 ± 1	0.37	−14.11	7.09	−9.35	0.29	1658 ± 3	45	73	0.18 ± 0.02	10.7	14.6	7.37	0.28
2094	14 19 29.08	35 34 01.10	ASK 392553	3207 ± 1	0.80	−16.38	8.39	−9.80	0.30	3185 ± 6	81	106	0.12 ± 0.03	6.1	7.5	7.78	−0.61
2099	14 20 11.10	10 15 46.50	NGC 5562	9142 ± 3	1.61	−21.84	11.40	−12.78	0.56	9187 ± 4	140	149	0.18 ± 0.07	3.4	4.4	8.87	−2.53
2140	14 28 08.70	01 49 25.60	ASK 082514	1728 ± 29	0.30	−14.29	–	–	0.29	1728 ± 3	25	43	0.08 ± 0.02	8.6	8.9	7.06	–
2225	14 45 36.30	34 10 43.80	ASK 394208	1642 ± 6	0.40	−14.51	7.15	−10.65	0.43	1630 ± 3	35	57	0.21 ± 0.03	10.8	13.2	7.42	0.27
2236^M	14 48 58.99	33 11 34.90	CGCG 193-002	1700 ± 2	0.70	−16.54	8.33	−9.97	0.50	1704 ± 2	50	77	0.64 ± 0.04	15.2	28.9	7.95	−0.38
2301^M	15 18 57.00	00 30 56.50	PGC 1168006	2082 ± 14	0.58	−14.59	7.51	−9.63	0.36	2098 ± 5	60	75	0.08 ± 0.03	3.8	4.4	7.21	−0.30
2311	15 24 50.10	03 04 53.10	SHOC 505	1753 ± 1	0.38	−14.87	7.56	−9.41	0.38	1745 ± 5	80	125	0.40 ± 0.04	11.2	19.3	7.77	0.22
2316	15 27 44.50	09 41 56.80	ASK 421256	1820 ± 1	0.51	−15.62	7.96	−9.67	0.41	1818 ± 3	46	78	0.56 ± 0.03	15.7	32.4	7.95	−0.01
2317	15 27 53.00	25 38 37.50	PGC 1744110	1470 ± 1	0.38	−13.64	6.91	−9.26	0.31	1477 ± 9	37	78	0.09 ± 0.03	6.8	8.1	6.99	0.09
2325^M	15 32 49.90	36 12 13.50	ASK 331970	1993 ± 1	0.54	−16.01	7.98	−9.56	0.50	2002 ± 3	48	68	0.21 ± 0.04	7.8	9.9	7.61	−0.37
2327	15 33 36.75	33 21 33.60	ASK 313250	1999 ± 2	0.36	−14.56	7.40	−9.43	0.41	1994 ± 8	52	93	0.19 ± 0.04	7.3	10.5	7.56	0.16
2349	16 00 13.80	17 50 53.80	PGC 1543427	2053 ± 1	0.46	−15.64	7.71	−9.42	0.51	2057 ± 3	79	106	0.59 ± 0.05	11.9	21.1	8.08	0.37
2373	16 35 20.70	17 45 55.10	Mrk 0886	2740 ± 1	0.63	−17.82	8.94	−9.52	0.34	2754 ± 5	86	129	0.39 ± 0.04	11.3	19.9	8.15	−0.79
2402	21 13 07.70	01 13 47.20	2MASX J21130776+0113480	4157 ± 2	0.75	−18.01	8.97	−9.78	0.70	4165 ± 10	146	187	0.49 ± 0.09	5.8	9.3	8.61	−0.36
2407^M	21 16 27.60	−00 49 35.30	NGC 7047	5783 ± 3	1.48	−20.60	10.71	−11.52	0.67	5796 ± 6	422	458	2.11 ± 0.14	8.4	24.7	9.53	−1.18
2410^M	21 17 34.60	11 00 43.20	ASK 138402	3271 ± 2	0.47	−15.37	7.50	−9.18	0.54	3266 ± 6	59	99	0.36 ± 0.05	9.4	14.3	8.27	0.77
2416	21 28 29.10	10 04 52.60	2MASX J21282910+1004527	4929 ± 2	1.02	−17.63	9.10	−10.14	0.65	4933 ± 5	178	192	0.32 ± 0.09	3.9	5.9	8.57	−0.53
2423	21 42 22.80	12 29 53.80	UGC 11794	5848 ± 4	1.42	−20.12	10.50	−11.28	0.46	5855 ± 6	344	384	1.22 ± 0.09	9.6	22.8	9.30	−1.19
2432	21 50 38.40	13 17 17.40	CGCG 427-027	6045 ± 2	1.50	−20.81	10.88	−11.40	0.60	6060 ± 6	208	231	0.41 ± 0.09	5.6	7.8	8.87	−2.02
2433	21 52 22.50	−01 10 15.70	ASK 21400	4770 ± 1	0.55	−16.57	8.14	−9.48	1.31	4753 ± 6	90	109	0.33 ± 0.13	4.2	4.3	8.55	0.41
2436	21 54 47.70	00 13 45.70	ASK 21641	2984 ± 1	0.48	−15.76	7.88	−9.47	0.43	2981 ± 4	73	107	0.47 ± 0.04	12.4	20.9	8.30	0.42
2452	22 26 19.50	12 15 02.00	ASK 140946	3527 ± 8	0.49	−15.59	7.72	−9.51	0.32	3544 ± 1	94	111	0.41 ± 0.03	12.9	20.9	8.39	0.67
2461	22 33 49.80	00 28 58.30	ASK 23755	4642 ± 1	0.47	−16.75	8.22	−9.39	0.89	4606 ± 22	59	161	0.52 ± 0.11	6.7	12.2	8.72	0.51
2534	23 25 30.20	14 06 20.50	ASK 144855	3996 ± 1	0.54	−15.91	7.91	−9.49	0.29	4001 ± 4	44	66	0.10 ± 0.02	8.0	8.2	7.87	−0.04

Table 2. Basic optical and Hɪ data – Arecibo marginal detections of Nançay non-detections.

Source	RA	Dec	Name	V_{opt}	$g-z$	M_g	$M_\star$	sSFR	rms	V_{HI}	W_{50}	W_{20}	F_{HI}	SNR	S/N	M_{HI}	$M_{HI}/M_\star$
	(J2000.0)			km s^{-1}	mag	mag	[log] $M_\odot$	[log] yr^{-1}	mJy	km s^{-1}	km s^{-1}	km s^{-1}	Jy km s^{-1}			[log] $M_\odot$	[log]
0345	03 04 57.96	00 57 14.10	SHOC 150	3636 ± 1	0.55	−16.02	–	–	0.61	3634 ± 3	25	34	0.05 ± 0.03	3.6	2.8	7.52	–
1132	10 56 19.90	17 05 05.90	PGC 4257755	960 ± 1	0.44	−12.53	6.57	−9.47	0.65	966 ± 12	17	37	0.03 ± 0.04	2.6	1.9	6.14	−0.43
1163	11 06 32.10	11 23 07.50	NGC 3524	1357 ± 1	1.32	−18.37	9.71	−11.27	0.74	1341 ± 8	415	431	0.23 ± 0.14	2.7	2.5	7.30	−2.40
1989	13 57 29.52	09 57 03.20	CGCG 074-017	6969 ± 2	1.30	−19.82	10.29	−11.92	0.51	6922 ± 10	317	344	0.21 ± 0.09	3.7	3.6	8.68	−1.61
2162	14 31 53.00	03 22 48.30	2MASX J23244466+0101490	1529 ± 1	0.64	−13.52	6.94	−9.37	0.47	1521 ± 5	24	38	0.03 ± 0.03	4.0	2.1	6.52	−0.43
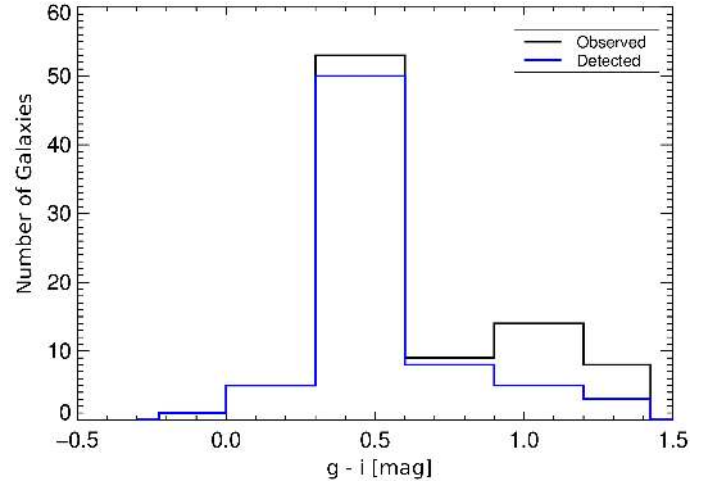
Fig. 1. Number of galaxies as a function of $g-i$ color, corrected for Galactic extinction following Schlegel et al. (1998). The black line is the total number of observed galaxies in each 0.25 mag wide bin and the blue line the total number of detected galaxies. The peak around 0.5 mag is due to our specific selection of blue objects (see Sect. 2).

5. Discussion

5.1. Arecibo detection rate of Nançay non-detections and marginal detections

In this section and the remainder of this paper we focus on the Arecibo follow-up sample consisting of the 90 galaxies observed at Arecibo which were either undetected or marginally detected at Nançay. The Nançay marginal detections are included with the Nançay non-detections for the analyses presented below since the marginal detection category had not yet been implemented at the time of this our Arecibo survey.

Of our 90 Nançay non-detections or marginal detections, 72 had sufficient Hɪ line flux to be clearly detected at Arecibo, resulting in a high overall detection rate of 80% (greater than 85% counting Arecibo marginal detections). One likely reason for this high detection rate is that most of our sample consisted of predominately blue, nearby star-forming galaxies. This color bias is obvious in Fig. 1, which shows the number of galaxies observed and detected as a function of $g-i$ color. All of the galaxies with $g-i$ colors bluer than 0.3 were detected, whereas only one third of the reddest galaxies were detected.

A color−magnitude diagram of integrated $g-i$ colors as a function of r-band luminosity is shown in Fig. 2 for our detections, non-detections, and marginals of both the Arecibo and the Nançay samples. The dichotomy in both color and luminosity between Hɪ detections and non-detections is obvious in this plot. At the low luminosity end ($\log(L_r) < 9$), the Nançay data show a color dichotomy with the detections clustering around $g-i \sim 0.4$ (commonly referred to as the "blue cloud") and non-detections clustering around $g-i \sim 0.8$ (commonly referred to as the "red sequence"). This dichotomy has not previously been seen in larger surveys such as Gavazzi et al. (2010) or Huang et al. (2012), primarily due to the smaller dynamic range probed by the former and by the exclusion of lower luminosity red galaxies in the latter. However, due to the NIBLES selection criteria and our ~1 dex larger dynamic range, our sample contains a clear separation by color at low luminosities.

The sole Arecibo non-detection in this low-luminosity range (inverted blue triangle in Fig. 2) has a relatively red color, but several other low-luminosity red sources were detected, and two
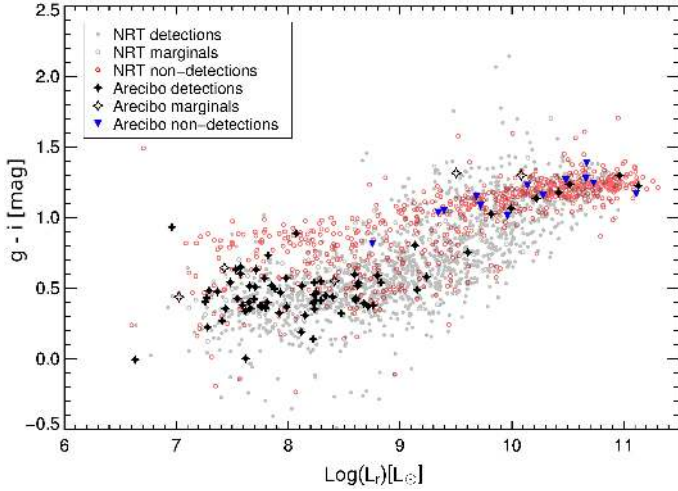
Fig. 2. Integrated $g - i$ color, in mag, as function of absolute r-band luminosity, $\log(L_r)$ in $L_\odot$, both corrected for Galactic extinction following Schlegel et al. (1998). Nançay detections, marginals, and non-detections are represented by gray dots, open gray circles, and open red circles respectively. Arecibo detections, marginals, and non-detections are respectively represented by black solid stars, open stars, and blue downward triangles. The low luminosity end ($\log(L_r) < 9$) shows a color dichotomy with Hɪ detections and non-detections clustering around $g - i \sim 0.4$ and $g - i \sim 0.8$ respectively, showing a clear distinction between the blue cloud and red sequence galaxies. Above luminosities of $\log(L_r) \sim 9.5$, the blue cloud disappears while the red sequence galaxies shift to redder colors, $g - i \sim 1.2$.

of the bluer low-luminosity galaxies were only marginally detected at Arecibo. Further follow-up of these red, low luminosity sources is needed to establish the Hɪ mass properties of this low-luminosity red population.

The blue cloud largely disappears at luminosities higher than $\log(L_r) = 9.5$, where the majority of sources cluster around $g - i$ color of ~ 1.2. However, aside from the fact that these galaxies have relatively more non-detections compared to the low luminosity galaxies, the mixture of detections with non-detections suggests that a not insignificant fraction of the red sequence galaxies may contain detectable levels of Hɪ. However, deeper follow-up observations of red sequence galaxies will be needed to answer this question.

We compare the detection fractions as a function of $g-i$ color and L_r for our Nançay and Arecibo samples in Fig. 3, counting the marginal detections in with the non-detections. The Nançay data show a global decrease in detection fraction as a function of color while the Arecibo data show a rather sharp drop by about a factor of 2.5 above $g - i \sim 0.8$. As a function of luminosity, the Nançay detection percentage shows no decrease below $\log(L_r) \sim$ 10 while the Arecibo sample shows a two times lower detection rate above $\log(L_r) \sim 9$. The plotted uncertainties in the Nançay data points are the standard deviation of the binomial distribution, given by

$$\sigma = \sqrt{\frac{P(1 - P)}{n}} \tag{3}$$

where P is the probability of detection, given by m/n where m is the number of detections and n is the total number in a particular bin. The Arecibo data generally have a small number of sources per bin which in some cases makes the uncertainty difficult to quantify. We therefore adopted the 90% confidence limits from
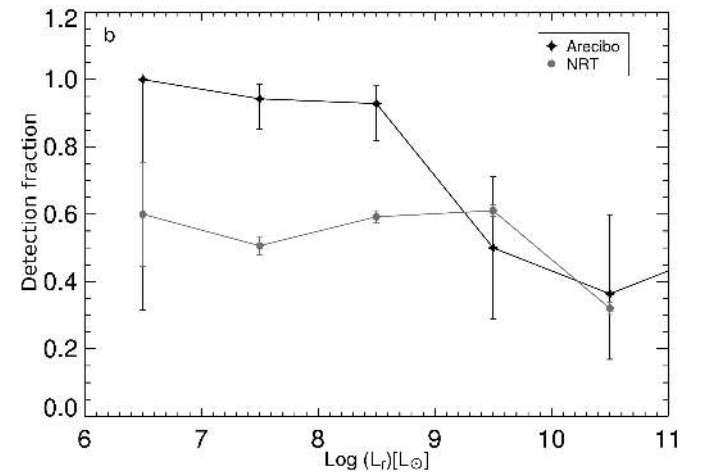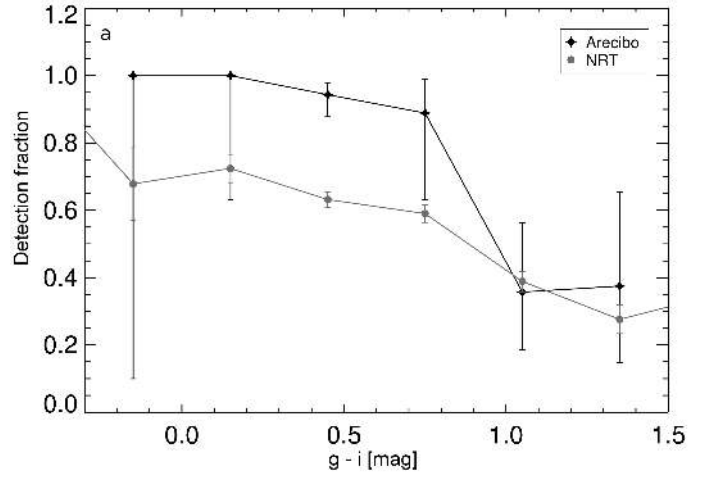

Fig. 3. a) Detection fraction for the NIBLES Nançay sample (gray) and the Arecibo follow-up sample (black) as a function of $g - i$ color. **b)** Detection fractions as a function of r-band luminosity. Error bars for the Nançay data are the standard deviation of the binomial distribution and the error bars for the Arecibo data were calculated following Gehrels (1986) using the 90% confidence intervals. Bin sizes are 0.3 for **a)** and 1 for **b)**.

Gehrels (1986) for dealing with the small number statistics of the Arecibo sample.

If we apply the Arecibo detection percentages to the Nançay sample, we would expect (with observations of the same sensitivity as our Arecibo sample, i.e., four times lower noise than at Nançay) to detect about 60% (or $\sim$530) of the 867 Nançay non-detections and marginal detections: based on color statistics the expected number is, 526 ± 160 and it is 546 ± 158 from the luminosity data (see Fig. 4). The uncertainty is calculated by adding in quadrature the fractional uncertainty in each $g - i$ or L_r bin, respectively.

We have a total remaining sample of 442 Nançay undetected or marginally detected galaxies within the Arecibo declination range, consisting mostly of redder low-luminosity (below $L_r \sim 10^9 L_\odot$) sources as well as some higher luminosity red sequence galaxies. Based on our current results, we estimate that comparable observations of the remaining 442 sources at Arecibo would require about 160 h of telescope time: 60% to be observed for our standard 5 min on-source integrations and the other 40% for 15 min each. If detection statistics follow the same pattern as this sample, we would expect about 60% of the remaining

Table 3. Basic optical and H I data – Arecibo non-detections.

| Source | RA | Dec | Name | V_{opt} | $g - z$ | M_g | $M_\star$ [log] | sSFR [log] | rms | SNR | M_{HI} [log] | $M_{HI}/M_\star$ [log] |
	(J2000.0)			km s^{-1}	mag	mag	$M_\odot$	yr^{-1}	mJy		$M_\odot$	
0879^K	09 34 02.80	10 06 31.30	NGC 2914	3144 ± 1	1.48	−19.80	10.37	−11.87	0.76	2.09	<8.89	<−1.45
0882^M	09 35 05.80	09 38 57.10	2MASX J09350578+0938566	3408 ± 2	1.27	−18.12	9.61	−11.36	0.61	2.80	<8.72	<−0.58
0906	09 41 16.60	10 38 49.10	IC 0552	5788 ± 2	1.57	−20.70	10.87	−12.11	0.64	2.95	<9.31	<−1.13
1076	10 36 38.40	14 10 15.90	NGC 3300	3017 ± 1	1.42	−20.24	10.53	−12.29	0.49	2.18	<8.56	<−1.45
1146	11 00 35.40	12 09 41.60	NGC 3491	6351 ± 2	1.59	−21.12	11.06	−12.65	0.56	2.29	<9.11	<−1.13
1224	11 21 24.90	03 00 50.10	NGC 3643	1742 ± 2	1.19	−17.98	9.53	−11.41	0.88	2.05	<8.35	<−1.05
1849	13 24 10.00	13 58 35.50	NGC 5129	6885 ± 2	1.45	−22.28	11.34	−12.51	0.58	1.47	<9.20	<−1.31
1893	13 38 43.10	31 16 13.90	CGCG 161-101	4699 ± 2	1.53	−19.85	10.52	−12.39	0.60	2.62	<9.07	<−1.17
1951	13 52 26.70	14 05 28.60	IC 0948	6892 ± 2	1.54	−21.33	11.14	−12.69	0.40	2.92	<9.01	<−1.31
2016^K	14 02 48.60	09 20 28.90	NGC 5423	5910 ± 2	1.47	−21.20	11.06	−12.67	0.47	2.80	<9.09	<−1.30
2401	21 04 51.99	00 26 52.70	CGCG 374-042	4129 ± 2	1.36	−18.88	9.95	−12.02	0.63	2.35	<8.95	<−0.34
2406	21 16 24.80	10 16 24.10	CGCG 426-029	5175 ± 2	1.26	−19.54	10.15	−11.09	0.59	2.19	<9.16	<−0.57
2418^M	21 31 37.60	11 49 53.90	CGCG 426-062	8643 ± 3	1.70	−21.05	11.15	−12.19	0.95	1.78	<9.87	<−0.98
2430	21 50 27.60	12 38 10.30	2MASX J21502753+1238103	6507 ± 2	1.42	−18.75	9.98	−11.69	0.62	2.64	<9.33	<−0.16
2442	22 04 08.80	−00 55 31.90	ASK 22153	4825 ± 16	0.82	−16.68	8.66	−10.35	0.15	3.14	<8.36	<0.86

Notes. Marginal and confused Nançay detections are flagged with an M and K respectively. The M_{HI} and $M_{HI}/M_\star$ columns list upper limit values.
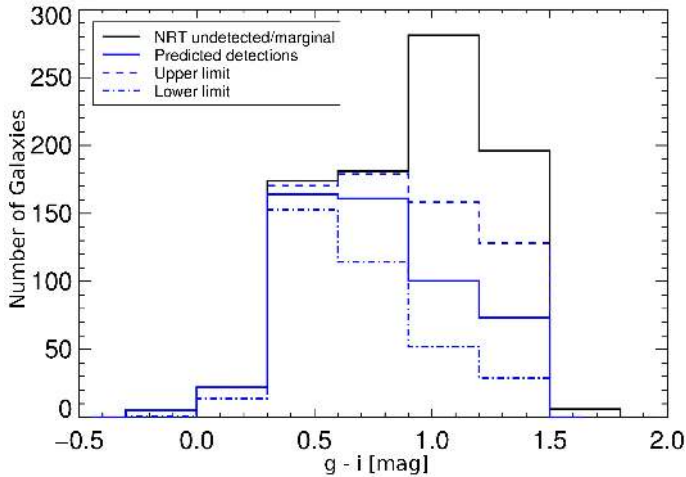

Fig. 4. Total number of galaxies either undetected or marginally detected at Nançay that would be detectable with the same sensitivity as our Arecibo observations, as a function of $g - i$ color. Black indicates Nançay non-detections and marginals, whereas the solid blue line is the estimated number of galaxies that would be detectable based on our Arecibo sample detection rate. The blue dashed and dash-dotted lines are based on, respectively, the upper and lower envelopes of the uncertainties in the detection rate, see Fig. 3.

Nançay undetected sample to be detected at Arecibo. This would bring the over-all detection rate of the NIBLES sample within the Arecibo declination range to ~89%, and the global detection rate to ~77%. If we extrapolate these detection percentages to the entirety of the NIBLES sample, we would expect the NIBLES global detection rate to increase to ~86%.

Of the subset of our sample that was selected on low luminosity and blue color, we achieved a 100% detection rate (including the Arecibo marginal detections). We also managed to detect several red sequence galaxies with very low H I stellar mass ratios, $\log(M_{HI}/M_\star) < -2$ (see Fig. 9). Two of these have stellar masses greater than $10^{11.5} M_\odot$, placing them in an area of $M_{HI}/M_\star - M_\star$ parameter space not probed by the ALFALFA survey and as yet virtually unexplored.

5.2. Physical properties of Arecibo-detected galaxies

In Paper I we used the $W_{20} - L_r$ relationship to estimate the maximum H I line width a galaxy typically has for a given luminosity. The least-squares fit to this relationship is $\log(W_{20}) = 0.4 + 0.2 \cdot \log(L_r)$. When comparing the Arecibo data to the Nançay data, the Arecibo detections appear to have W_{20} values that are about 35% narrower than the corresponding Nançay detections of the same luminosity. This is due in large part to our selection of low luminosity blue dwarf galaxies, which are predominately supported by velocity dispersion rather than rotation. Consequently, the H I line profiles of these galaxies are typically Gaussian shaped rather than displaying the commonly seen two-horned profiles. Since these galaxies make up ~70% of our Arecibo detections, they are primarily responsible for this offset. To illustrate this effect, we subtract the fit to the $W_{20} - L_r$ relationship from each source in the range $\log(L_r) \leq 8.5$ and plot the resulting distributions for both the Nançay and Arecibo data in Fig. 5. The mean and standard deviations of the Nançay and Arecibo distributions are 7 ± 36 and -22 ± 20 km s^{-1} respectively. As is evident, the majority of the line widths for the Arecibo sample lie below the mean fit of the Nançay sample and have a much narrower distribution.

To see if this difference in H I line profile width corresponds to any differences in over-all stellar distribution, we examine the distributions of r-band half-light radius. Here we define the half-light radius as the R_{50} radius encompassing 50% of the Petrosian flux, scaled for the Hubble-flow distance to the galaxy. This radius gives a general sense of the stellar mass concentration within a galaxy under the assumption that the mass-to-light ratios of galaxies of the same luminosity are fairly consistent. To test this assumption, we examined the distribution of g-r colors between the low luminosity ($\log(L_r) \leq 8.5$) Arecibo and NRT samples and found no significant difference (a Kolmogorov-Smirnov (K-S) test returns a 49.4% probability that these distributions are not drawn from the same parent sample). The similarities in color distribution between the two samples indicates that they do not have vastly differing stellar populations. Therefore, differences in half-light radius should indicate differences in compactness.

We plot the half-light radius distribution of the two samples in Fig. 6, which shows that the Arecibo data are systematically

Table 4. Basic optical and HI data – comparison of Arecibo and Nançay detections.

Source Telescope	RA (J2000.0)	Dex	Name	V_{opt} km s^{-1}	$g-z$ mag	M_g mag	$M_\star$ [log] $M_\odot$	sSFR [log] yr^{-1}	rms AO mJy	rms NRT mJy	V_{HI} AO km s^{-1}	V_{HI} NRT km s^{-1}	W_{50} AO km s^{-1}	W_{50} NRT km s^{-1}	F_{HI} AO Jy km s^{-1}	F_{HI} NRT Jy km s^{-1}	S/N AO	S/N NRT	M_{HI} AO [log] $M_\odot$	M_{HI} NRT [log] $M_\odot$
0047	00 20 48.60	14 13 27.80	2MASX J00204857+1413283	5344 ± 1	0.91	−18.34	9.31	−9.51	0.61	1.69	5348 ± 7	5260 ± 7	107	55	0.65 ± 0.07	0.3 ± 0.1	16.51	4.03	8.95	8.63
0337	02 59 14.50	00 33 59.70	ASK 37367	2754 ± 2	0.18	−15.42	8.12	–	0.59	2.21	2760 ± 1	2727 ± 11	53	56	1.17 ± 0.05	0.5 ± 0.2	44.25	4.76	8.63	8.24
0576	08 01 58.90	21 22 19.10	ASK 363290	2089 ± 3	0.54	−14.98	–	–	0.61	2.16	2087 ± 6	2058 ± 6	77	91	0.70 ± 0.06	0.6 ± 0.2	20.94	4.70	8.16	8.08
0613^K	08 17 53.93	24 41 12.00	ASK 363797	2065 ± 2	−0.25	−14.52	7.14	−8.98	0.53	1.54	2069 ± 2	2030 ± 2	49	134	1.83 ± 0.05	10.1 ± 0.2	79.47	93.39	8.58	9.31
0619^{C3}	08 18 19.70	24 31 36.90	IC 2271	2213 ± 2	0.45	−17.07	8.29	−9.43	0.66	3.58	2227 ± 4	2208 ± 3	74	68	2.47 ± 0.07	2.0 ± 0.3	70.80	11.28	8.77	8.68
0648	08 24 17.99	20 30 49.40	ASK 522889	2166 ± 3	0.69	−16.44	7.69	−9.32	0.51	2.51	2170 ± 5	2146 ± 22	78	121	0.76 ± 0.06	0.9 ± 0.3	27.66	5.58	8.24	8.32
0717	08 44 28.60	31 21 23.40	ASK 282097	2200 ± 5	0.50	−15.63	7.84	−9.55	0.55	2.95	2199 ± 1	2175 ± 6	140	135	2.57 ± 0.07	1.8 ± 0.3	64.31	8.56	8.78	8.61
0769	08 58 00.60	25 41 52.40	ASK 486934	1897 ± 0	0.34	−15.13	7.43	−9.19	0.56	2.90	1888 ± 2	1878 ± 7	78	75	0.69 ± 0.05	0.7 ± 0.3	22.33	4.30	8.07	8.05
0827	09 14 48.80	33 01 15.30	2MASX J09144880+3301148	1819 ± 2	0.59	−16.25	8.12	−9.49	0.57	2.95	1819 ± 9	1805 ± 8	46	76	0.40 ± 0.06	0.4 ± 0.3	16.66	2.75	7.80	7.83
0854	09 21 14.99	09 43 52.20	ASK 293255	1383 ± 2	0.65	−13.92	7.24	−9.62	0.57	2.45	1373 ± 4	1351 ± 4	46	48	0.16 ± 0.04	0.3 ± 0.3	6.61	2.55	7.15	7.37
0877^{CKR}	09 33 46.10	10 09 09.00	NGC 2911	3231 ± 2	1.73	−20.46	11.04	−13.08	0.79	1.60	3205 ± 22	3106 ± 67	422	314	4.72 ± 0.19	2.3 ± 0.4	47.42	13.63	9.37	9.05
1000	10 12 52.80	22 43 19.20	CGCG 123-024	1281 ± 3	0.80	−16.05	8.16	−9.73	0.64	3.08	1293 ± 2	1277 ± 6	109	104	1.27 ± 0.07	0.6 ± 0.3	30.83	3.10	8.01	7.67
1025^K	10 18 10.30	07 08 34.70	ASK 230324	3779 ± 2	0.68	−17.39	8.71	−9.80	0.81	2.68	3777 ± 8	3666 ± 17	121	184	1.55 ± 0.11	4.8 ± 0.4	28.04	21.65	9.03	9.50
1047	10 25 46.40	05 39 06.70	CGCG 037-033	1154 ± 2	0.35	−14.88	7.38	−10.54	0.55	2.24	1155 ± 1	1146 ± 8	97	102	2.89 ± 0.06	2.4 ± 0.3	86.72	17.31	8.27	8.18
1126	10 54 21.90	27 14 22.10	NGC 3451	1356 ± 1	1.04	−18.19	–	–	0.63	2.55	1335 ± 1	1326 ± 3	238	235	7.27 ± 0.10	6.1 ± 0.4	122.40	25.90	8.80	8.72
1156^K	11 03 59.80	27 56 16.10	PGC 4571781	1424 ± 2	0.69	−13.45	6.99	−9.70	0.65	2.28	1413 ± 17	1366 ± 42	103	191	0.64 ± 0.09	4.4 ± 0.3	15.64	22.93	7.79	8.60
1161	11 05 32.50	17 38 22.50	2MASX J11053253+1738228	1039 ± 2	0.75	−16.24	8.30	−10.00	0.77	1.56	1042 ± 1	1030 ± 5	97	95	2.06 ± 0.08	1.6 ± 0.2	44.29	16.92	8.03	7.90
1188	11 22 39.80	09 03 21.00	IC 0676	1412 ± 3	1.37	−18.26	9.69	−10.30	1.27	1.85	1433 ± 7	1430 ± 26	188	145	1.66 ± 0.18	1.2 ± 0.3	15.57	8.81	8.21	8.07
1238^K	11 22 50.70	12 20 41.50	IC 2781	1547 ± 1	0.44	−15.17	7.45	−9.35	0.61	2.39	1546 ± 2	1558 ± 13	82	106	1.26 ± 0.06	1.4 ± 0.3	36.95	9.50	8.16	8.22
1242	11 23 07.00	30 28 44.10	KUG 1120+307	1610 ± 1	0.61	−16.73	8.27	−9.48	0.57	3.27	1617 ± 2	1611 ± 9	104	95	2.86 ± 0.06	2.6 ± 0.4	79.80	13.26	8.56	8.51
1291	11 31 08.90	13 34 13.40	ASK 433348	1019 ± 2	0.40	−13.31	6.77	−9.29	0.74	1.09	1021 ± 2	1010 ± 5	38	50	0.49 ± 0.05	0.3 ± 0.1	17.30	6.11	7.39	7.15
1296	11 31 44.60	34 20 00.20	UGC 06512	1871 ± 3	0.58	−17.87	8.69	−9.56	0.75	1.81	1866 ± 1	1853 ± 9	155	154	9.32 ± 0.09	8.1 ± 0.2	161.74	60.00	9.19	9.13
1349^K	11 41 29.80	32 20 59.50	Mrk 0746	1804 ± 1	0.31	−16.69	7.94	−9.16	0.60	3.05	1842 ± 5	1806 ± 4	107	129	3.60 ± 0.07	8.4 ± 0.4	94.92	39.99	8.77	9.12
1426	11 54 01.60	16 43 24.00	PGC 166116	983 ± 1	−0.43	−13.59	7.04	−9.45	0.57	2.76	978 ± 1	970 ± 4	32	35	0.89 ± 0.04	0.8 ± 0.2	44.28	8.55	7.61	7.59
1427	11 54 04.40	30 06 34.60	PGC 4301309	980 ± 9	0.18	−13.61	6.76	−9.41	0.54	3.56	970 ± 1	968 ± 2	68	69	2.93 ± 0.05	2.4 ± 0.3	108.38	13.33	8.12	8.03
1501	12 04 04.50	28 58 58.20	KUG 1201+292	920 ± 1	0.78	−15.58	–	–	0.46	1.17	912 ± 2	908 ± 14	69	62	0.69 ± 0.04	0.5 ± 0.1	29.26	8.16	7.44	7.26
1528	12 08 24.20	03 00 47.90	ASK 075814	880 ± 2	0.64	−12.39	6.58	−9.56	0.78	1.75	884 ± 4	859 ± 6	31	33	0.10 ± 0.05	0.2 ± 0.1	3.80	2.70	6.58	6.77
1572	12 13 48.30	12 41 25.90	IC 3052	812 ± 14	0.38	−13.60	7.03	−10.16	0.64	3.59	847 ± 1	834 ± 9	61	85	0.67 ± 0.05	0.7 ± 0.3	21.98	3.27	7.36	7.34
1625	12 21 07.00	00 27 40.80	ASK 570	1894 ± 1	0.27	−14.81	7.20	−8.96	0.72	1.60	1890 ± 4	1875 ± 7	39	49	0.43 ± 0.06	0.4 ± 0.1	15.50	5.54	7.87	7.81
1631^R	12 22 03.90	09 02 05.60	NGC 4307	962 ± 14	1.63	−17.74	7.94	–	0.53	1.79	1053 ± 2	1055 ± 20	310	331	1.16 ± 0.09	1.2 ± 0.3	20.56	6.09	7.79	7.81
1633	12 22 08.20	15 47 56.40	VCC 0530	1301 ± 10	−0.08	−14.91	–	–	0.65	1.51	1296 ± 1	1288 ± 1	36	42	0.60 ± 0.05	0.6 ± 0.1	24.92	10.64	7.69	7.71
1790	13 05 18.80	36 06 10.40	IC 4171	1201 ± 3	0.48	−15.62	7.71	−9.93	0.77	2.94	1206 ± 1	1197 ± 2	115	111	4.99 ± 0.08	3.8 ± 0.3	98.61	20.36	8.54	8.42
1897	13 39 22.34	31 14 57.60	ASK 526959	703 ± 2	0.28	−13.50	6.72	−9.14	0.48	2.45	702 ± 2	694 ± 3	41	51	2.17 ± 0.04	1.8 ± 0.2	115.15	16.92	7.71	7.62
2068	14 12 58.55	09 55 15.90	CGCG 074-140	7054 ± 2	1.26	−20.11	10.32	−9.94	0.49	1.79	7079 ± 2	6910 ± 11	290	291	1.80 ± 0.08	1.6 ± 0.3	34.94	8.60	9.64	9.59
2176	14 35 33.30	12 54 29.60	UGC 09389	1835 ± 2	0.67	−17.92	8.86	−10.16	0.40	1.34	1826 ± 1	1811 ± 0	229	230	16.32 ± 0.06	14.4 ± 0.2	438.20	117.39	9.42	9.36
2178	14 35 50.10	02 36 19.70	ASK 83319	1569 ± 2	0.47	−15.23	6.18	–	0.50	3.48	1557 ± 1	1550 ± 5	63	56	2.19 ± 0.04	1.8 ± 0.3	89.09	11.68	8.41	8.33
2224	14 45 33.60	31 54 56.10	ASK 470206	1208 ± 14	−0.61	−13.60	7.12	−10.73	0.62	1.91	1212 ± 1	1203 ± 5	74	75	0.94 ± 0.06	0.9 ± 0.2	28.84	8.56	7.82	7.78
2247	14 52 43.50	11 40 19.90	ASK 417578	1803 ± 4	0.63	−15.32	7.75	−9.44	0.54	3.40	1802 ± 1	1784 ± 5	123	109	2.10 ± 0.06	1.5 ± 0.4	57.57	7.09	8.52	8.37

Notes. AO = Arecibo, NRT = Nançay. Flags used in column Source: C for clear confusion with another galaxy within the Nançay telescope beam, $C3$ for another galaxy in the beam that is unlikely to cause confusion and K for sources confused within the Nançay telescope beam.

Table 4. continued.

Source Telescope	RA	Dex (J2000.0)	Name	V_{opt} [km s^{-1}]	$g-z$ [mag]	M_g [mag]	$M_\star$ [log $M_\odot$]	sSFR [log yr^{-1}]	rms AO [mJy]	rms NRT [mJy]	V_{HI} AO [km s^{-1}]	V_{HI} NRT [km s^{-1}]	W_{50} AO [km s^{-1}]	W_{50} NRT [km s^{-1}]	F_{HI} AO [Jy km s^{-1}]	F_{HI} NRT [Jy km s^{-1}]	S/N AO	S/N NRT	M_{HI} AO [log $M_\odot$]	M_{HI} NRT [log $M_\odot$]
2341	15 55 22.40	02 55 15.10	ASK 104991	1998 ± 7	0.30	−14.44	7.23	−9.54	0.50	2.90	2002 ± 1	1993 ± 8	65	72	0.67 ± 0.04	0.6 ± 0.3	26.84	3.91	8.11	8.05
2414	21 23 18.40	01 15 18.10	2MASX J21231841+0115175	5458 ± 2	1.51	−18.72	10.08	−10.43	0.90	1.51	5467 ± 9	5397 ± 21	236	227	1.32 ± 0.14	1.1 ± 0.2	15.46	7.68	9.28	9.19
2417^K	21 30 25.88	−00 28 27.70	2MASX J21302589-0028272	5964 ± 2	1.48	−18.56	9.91	−10.10	0.67	1.74	6008 ± 5	5905 ± 21	267	269	2.00 ± 0.11	2.6 ± 0.3	29.54	15.12	9.54	9.66
2419	21 35 03.60	10 57 36.20	ASK 138954	3490 ± 7	0.63	−16.60	8.06	−9.60	0.30	2.30	3502 ± 1	3465 ± 35	128	96	0.77 ± 0.03	0.6 ± 0.3	37.06	4.53	8.66	8.57
2421	21 41 11.20	12 43 15.80	ASK 139485	6206 ± 3	0.52	−17.81	8.81	−9.72	0.49	1.50	6207 ± 1	6080 ± 13	161	139	0.64 ± 0.06	0.7 ± 0.2	16.60	6.52	9.08	9.12
2428	21 45 22.60	12 16 06.30	ASK 139520	5776 ± 4	0.36	−16.80	8.21	−9.41	0.56	1.73	5799 ± 3	5689 ± 8	118	148	0.49 ± 0.06	0.4 ± 0.2	12.87	3.46	8.90	8.86
2434^{CKD}	21 52 37.90	12 32 09.00	CGCG 427-032	8724 ± 1	1.83	−20.88	11.16	−11.90	1.49	2.58	8540 ± 13	8469 ± 7	93	139	1.01 ± 0.18	0.5 ± 0.3	11.11	2.76	9.55	9.28
2435	21 54 17.99	00 56 31.50	2MASX J21541799+0056318	2976 ± 1	0.42	−17.39	8.36	−9.18	0.61	2.73	2991 ± 8	2943 ± 10	138	186	1.58 ± 0.09	1.2 ± 0.4	35.68	5.36	8.83	8.71
2439	22 00 44.10	12 18 03.00	ASK 140028	8800 ± 1	0.27	−18.13	6.89	−9.45	0.47	1.70	8785 ± 6	8544 ± 5	128	142	1.07 ± 0.06	0.9 ± 0.2	32.10	6.90	9.60	9.51
2441	22 03 15.99	00 34 15.90	NGC 7189	9020 ± 1	1.45	−21.51	11.10	−10.63	0.63	3.00	9054 ± 3	8774 ± 38	391	393	2.58 ± 0.12	3.2 ± 0.6	33.29	8.79	10.01	10.10
2449^{CK}	22 21 33.70	12 31 22.30	ASK 140519	7771 ± 1	0.89	−18.50	–	–	0.46	1.79	7769 ± 5	7578 ± 13	405	364	1.86 ± 0.09	1.8 ± 0.3	32.30	8.63	9.73	9.72
2450	22 22 08.80	12 04 24.10	ASK 141077	5125 ± 4	0.71	−16.44	8.68	−9.46	0.53	1.53	5108 ± 1	5026 ± 11	155	149	1.20 ± 0.07	0.8 ± 0.2	29.02	6.81	9.18	8.99
2464	22 39 31.31	−00 40 36.10	ASK 23608	7728 ± 3	0.58	−17.19	–	–	0.82	1.83	7719 ± 2	7507 ± 11	158	146	0.99 ± 0.10	0.6 ± 0.2	15.44	4.33	9.45	9.23
2469^K	22 40 57.58	−01 15 08.70	PGC 1123197	4747 ± 3	1.48	−18.99	10.10	−11.15	0.77	1.33	4760 ± 5	4734 ± 9	78	211	0.36 ± 0.07	0.7 ± 0.2	8.46	5.58	8.59	8.86
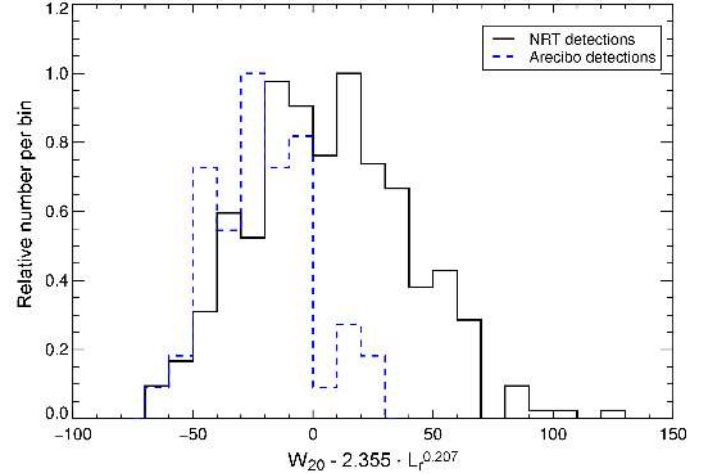
Fig. 5. Relative number of galaxies per bin for the Nançay and Arecibo samples as a function of the difference in W20 with fit to the $W_{20}-L_r$ relationship, i.e., $W_{20}-2.355 \cdot L_r^{0.207}$ with a bin size of 10.
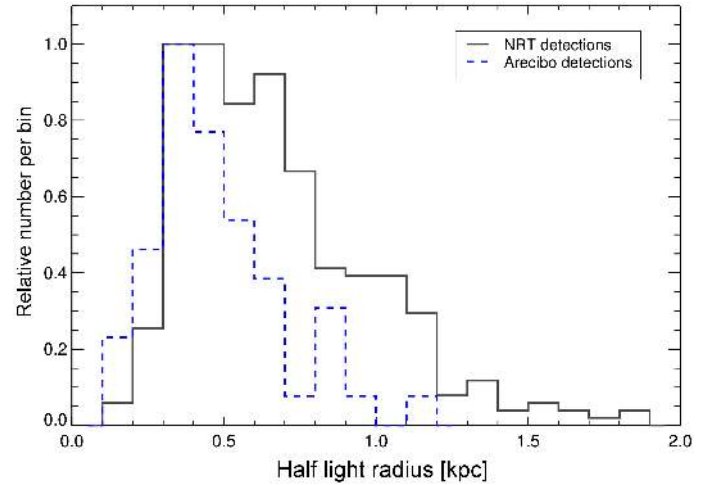

Fig. 6. Relative number of galaxies per bin of the Nançay and Arecibo samples as a function of half-light radius, in kpc. Bin size is 100 pc.

offset to lower radii than the Nançay data. The mean and standard deviations are 0.68 ± 0.32 kpc for Nançay and 0.47 ± 0.22 kpc for Arecibo. A K-S test returns a 94% probability that the Nançay and Arecibo samples are not drawn from the same parent distribution.

The smaller half-light radii of the Arecibo sample, combined with the fact that these galaxies have narrower H I line widths, on average, may indicate that these galaxies are indeed more compact. Since dwarf galaxies tend to have rotation curves that increase with radius, the narrow H I line widths of these galaxies may be an indicator that the H I is being confined to the central regions of the galaxy. If this is the case, it may imply that these galaxies are in a different phase of evolution than their Nançay detected counterparts. However, further investigation is necessary.

In Fig. 7 we show the integrated H I line flux as a function of the W_{50} line width for both our Arecibo and Nançay non-confused and non-resolved detections and marginals, together with the ALFALFA detections and marginals from Haynes et al. (2011) for comparison. We also indicate the line flux for a flat-topped 3σ detection with the mean Arecibo rms noise level of 0.57 mJy, to show where weak detections are expected to lie.

Table 5. Basic optical and HI data – Arecibo detected galaxies not included in the final Nançay sample.

Source	RA	Dec	Name	V_{opt}	$g-z$	M_g	$M_\star$ [log]	sSFR [log]	rms	V_{HI}	W_{50}	W_{20}	F_{HI}	SNR	S/N	M_{HI} [log]	$M_{HI}/M_\star$ [log]
	(J2000.0)			km s^{-1}	mag	mag	$M_\odot$	yr^{-1}	mJy	km s^{-1}	km s^{-1}	km s^{-1}	Jy km s^{-1}			$M_\odot$	$M_\odot$
2601	01 21 02.95	00 51 05.30	ASK 032535	2438 ± 1	0.43	−15.61	7.71	−9.40	0.88	2433 ± 6	25	37	0.06 ± 0.05	2.6	2.0	7.20	−0.51
2602	08 17 07.90	24 33 45.70	ASK 363798	2127 ± 2	0.42	−15.27	6.30	−9.65	0.52	2126 ± 1	63	79	1.39 ± 0.04	18.1	54.6	8.48	2.18
2603	08 18 50.20	22 06 55.30	CGCG 119-044	3484 ± 2	0.58	−17.88	8.74	−9.53	0.63	3494 ± 1	124	138	1.88 ± 0.07	16.2	43.1	9.04	0.31
2604	08 46 47.29	13 42 24.40	CGCG 061-011	2141 ± 3	0.77	−16.59	8.47	−9.89	0.55	2142 ± 1	66	89	1.46 ± 0.05	18.1	52.8	8.51	0.04
2605	08 52 31.44	00 51 12.80	ASK 058363	3252 ± 1	0.62	−15.41	7.81	−9.70	0.48	3259 ± 3	80	95	0.13 ± 0.04	6.2	4.8	7.81	0.01
2606	11 37 48.50	22 41 28.60	NGC 3772	3551 ± 2	1.42	−19.75	10.35	−11.73	0.39	3423 ± 7	112	137	0.16 ± 0.04	4.8	6.2	7.95	−2.40
2607	11 40 13.90	24 41 49.40	NGC 3798	3567 ± 2	1.47	−20.39	10.61	−10.70	0.74	3552 ± 4	389	415	1.97 ± 0.14	9.8	21.9	9.08	−1.53
2608	14 18 53.47	09 17 28.70	ASK 456832	1201 ± 1	−1.17	−13.37	6.94	−9.40	0.28	1208 ± 2	49	71	0.28 ± 0.02	14.0	23.5	7.30	0.36
2609	14 45 20.20	34 19 48.10	ASK 394205	1666 ± 5	0.38	−14.83	7.35	−9.25	0.61	1668 ± 2	45	75	0.84 ± 0.05	16.5	33.6	8.05	0.71
2610	21 30 59.86	−00 00 02.10	CGCG 375-048	9034 ± 3	0.95	−20.72	10.22	−10.55	0.97	9052 ± 2	228	252	3.36 ± 0.15	13.7	36.6	10.12	−0.09

Notes. Sources which were excluded from the original data release in Paper I due to observational problems.
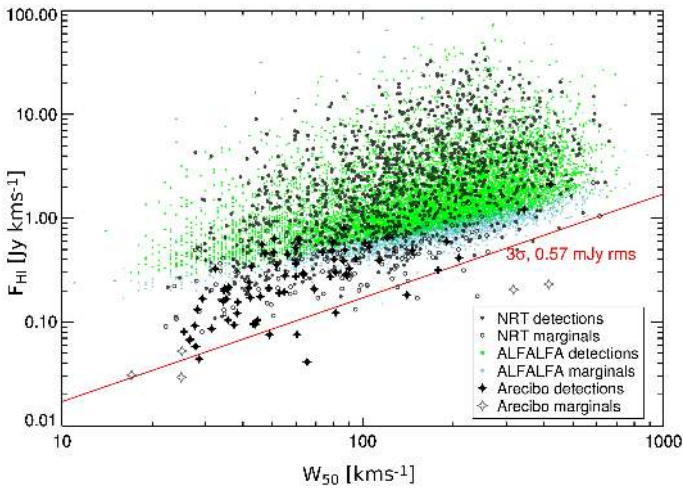
Fig. 7. Integrated HI line flux F_{HI} (in Jy km s^{-1}) as a function of W_{50} line width (in km s^{-1}). Shown are the NIBLES non-confused and non-resolved detections and marginals from both our Arecibo and Nançay observations, together with the ALFALFA data from the $\alpha.40$ catalog (Haynes et al. 2011), where green dots represent detections (their Category 1) and light blue dots represent marginals (Category 2). The red line indicates the integrated line flux from a 3σ flat-topped profile with a 0.57 mJy rms noise level.

The ALFALFA data show an increasingly marked absence of weak sources with decreasing line width, beginning at about $W_{50} \sim 100$ km s^{-1}. This is due to both the detection threshold of ALFALFA (see Giovanelli et al. 2005) and the fact that blind surveys have no a priori knowledge of source redshifts. In the NIBLES observations, prior knowledge of the source redshift enables us to identify signals to a lower SNR.

Figure 8 shows HI masses as a function of radial velocity for the same sources shown in Fig. 7. Additionally, we recalculated the HI masses of the ALFALFA galaxies using pure Hubble-flow distances in order to maintain consistency with the NIBLES calculations. The green vertical arrow represents the 0.16 dex average offset in HI mass due to difference in flux scale between the $\alpha.40$ catalog and our NRT data discussed in Paper I.

In Fig. 9 we compare the HI mass fraction $\log(M_{HI}/M_\star)$ as a function of stellar mass ($\log(M_\star)$), showing our Nançay (NRT) detections and marginals, ALFALFA detections, and our Arecibo sample detections, marginals, and upper limits for the non-detections. Our Arecibo upper limits were calculated following the same method used in Paper I, i.e., using a line width estimate from the upper envelope of the $W_{20}-L_r$ relationship.
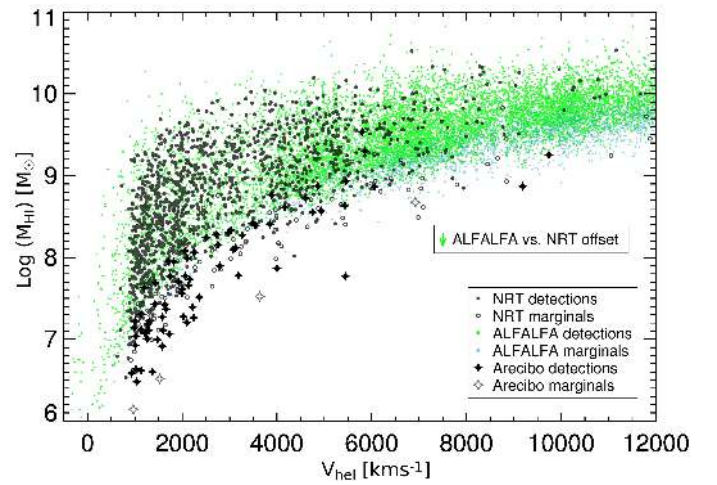

Fig. 8. Total HI mass, M_{HI} (in $M_\odot$), as a function of HI radial velocity (in km s^{-1}). Shown are the NIBLES detections and marginals from both our Arecibo and Nançay observations (black stars and dots respectively), together with data based on the ALFALFA $\alpha.40$ catalog (Haynes et al. 2011), where green dots represent detections (their Category 1) and light blue dots represent marginals (Category 2). Excluded were all NIBLES detections which are definitely or probably confused by another galaxy within the telescope beam, as well as detections that are likely resolved (see Paper I). The HI masses of the ALFALFA detections were calculated in the same way as for the NIBLES sources, using simply a distance of $D = V/H_0$, where the adopted Hubble constant is $H_0 = 70$ km s^{-1} Mpc^{-1}. The green vertical arrow above the legend indicates the difference of 0.16 in $\log(M_{HI})$ corresponding to the mean HI flux scale difference between the $\alpha.40$ catalog and our NRT data.

For ALFALFA, we also took the stellar mass estimates from the DR9 added-value MPA-JHU catalogs for consistency with the NIBLES sample (see Paper I).

The distribution of $\log(M_{HI}/M_\star)$ vs. $\log(M_\star)$ data shows the same general trend as presented in Paper I and Papastergis et al. (2012), with the HI-selected galaxy samples lying at systematically higher HI mass fractions for a given stellar mass than the optically selected NIBLES galaxies. We note that Papastergis et al. (2012) used their own method for estimating the stellar masses of their sample (see Huang et al. 2012, for details). As mentioned in Paper I, the ALFALFA fluxes are systematically higher than ours by a factor of 1.45 due to flux scale differences (see the 0.16 dex vertical green arrow in Fig. 9). However, even taking this offset into account, the HI-selected sample is has systematically higher $M_{HI}/M_\star$ ratios for a given $M_\star$ than NIBLES.
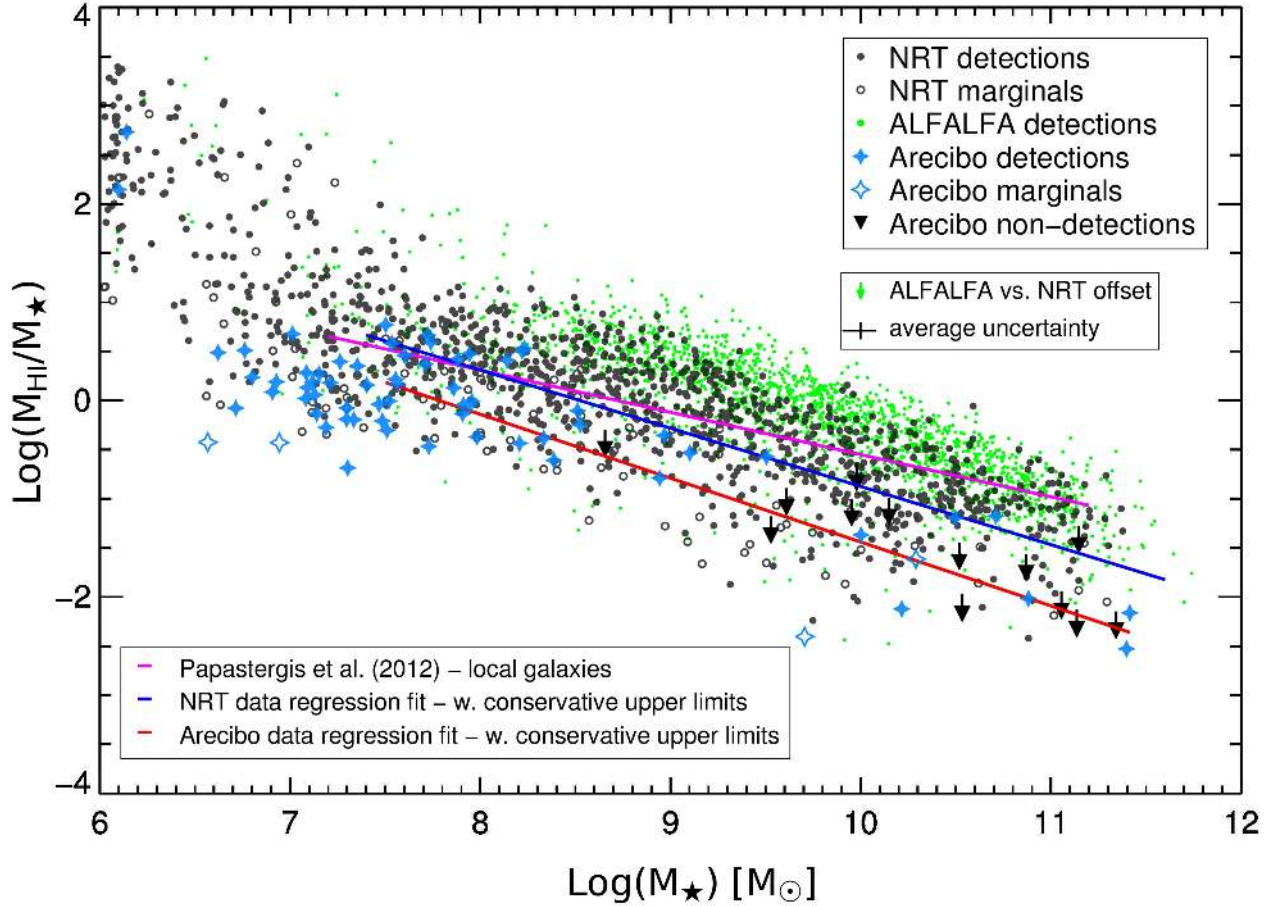
Fig. 9. H I mass fraction ($M_{HI}/M_\star$) as a function of total stellar mass, $M_\star$ (in $M_\odot$). NIBLES Nançay detections and marginals are represented by gray dots and open circles respectively while ALFALFA detections are represented by green dots. Our follow-up Arecibo detections and marginals are represented by solid and open light blue stars respectively while upper limits for non-detections are shown as downward arrows. Stellar masses used were taken from the SDSS added-value MPA-JHU catalogs (see Sect. 4). The green arrow below the legend represents the 0.16 dex average offset between the ALFALFA and NIBLES H I masses due to flux scale differences and the black cross indicates the average uncertainty in the stellar masses and mass fractions (about 20% in both cases). The magenta line represents the fit to literature reference samples of H I-detected galaxies from Papastergis et al. (2012), the blue and red lines represent the regression fits to the Nançay and Arecibo sources, respectively, which include estimated upper limits to H I masses of undetected galaxies (see Paper I for further details).

To assess the parameter space probed by our Arecibo sample, we also compare the literature fit made in Papastergis et al. (2012) of the four reference samples with H I detections they used to evaluate the gas-to-stellar mass ratios of local galaxies (magenta), with fits to our data. We used the Buckley-James method of linear regression, taking into account the H I non-detections, from the STSDAS statistics package[1] to fit the Nançay (blue line) and Arecibo (red line) samples (see also Paper I). Since the $\log(M_{HI}/M_\star)$ vs. $\log(M_\star)$ relationship becomes non-linear below $\log(M_\star) \sim 10^{7.5}$, we only include masses above this cut-off in our fits. Average uncertainties for each Arecibo source are represented by the cross below the legend. We estimate a mean 1σ stellar mass uncertainty of about 20%, based on Kauffmann et al. (2003), and a typical uncertainty of about 20% for the NIBLES Arecibo gas mass fractions. Our typical gas mass fraction uncertainty for the entire NIBLES sample is about 27% (see Paper I for details).

As mentioned in Paper I, there is an increasing discrepancy between the Papastergis et al. (2012) reference sample H I mass fraction (magenta) and the Nançay mass fraction (blue)

as a function of increasing stellar mass. When comparing our Arecibo sample to the Nançay and Papastergis et al. (2012) samples, we see the Arecibo sample follows roughly the same trend as the Nançay data but with an approximately 0.5 dex offset toward lower H I mass fractions. From Paper I, the Nançay regression fit is $\log(M_{HI}/M_\star) = -0.59 \log(M_\star) + 5.05$ and the Arecibo fit is $\log(M_{HI}/M_\star) = -0.65 \log(M_\star) + 5.06$. Since the Arecibo sample is a small fraction of the total NIBLES sample, we only show this fit here to illustrate the differences in H I mass fractions of the Nançay undetected sample. If this trend is representative of the rest of the NIBLES Nançay undetected galaxies, we would expect the NRT regression fit to be offset toward lower mass fractions by about 0.17 dex. Taking the entire stellar mass range into account and comparing mean H I mass fraction values in 0.2 mag wide bins in $\log(M_\star)$, we find that on average the Arecibo sample probes mass fractions that are 0.5 and 1 dex lower in $\log(M_{HI})$ than the Nançay and ALFALFA detections, respectively.

6. Conclusions

We obtained about four times more sensitive follow-up H I observations at Arecibo of 90 NIBLES galaxies that were either

---

[1] http://stsdas.stsci.edu/cgi-bin/gethelp.cgi?statistics

not detected or marginally detected at Nançay. We detected 80% of these sources, which has enabled us to probe their underlying H I distribution. The Arecibo detections have on average five times lower H I masses than the Nançay upper limits estimated in Paper I. Contributing to this factor of five lower mass is not only the lower peak flux densities we are able to detect with Arecibo, but also the ∼37% narrower line widths in our follow-up sample compared to the Nançay detections of sources with the same optical luminosity. This average difference in line width is primarily driven by the low luminosity ($L_r < 10^{8.5}$ $L_\odot$) sources which correspondingly show a higher central concentration of light. This may be an indication that these relatively gas-poor galaxies have, on average, a more centrally confined H I mass distribution compared to the Nançay detected sample in the same luminosity range.

If we assume the $g - i$ color and L_r distribution of Arecibo detection fractions are representative of the entire Nançay undetected and marginally detected samples, we estimate ∼60% (520) could be detected with the four times better sensitivity of our Arecibo observations. This would put the over-all NIBLES detection rate at about 86%.

Lastly, our Arecibo follow-up observations enabled us to sample our Nançay undetected sample to H I mass fractions 0.5 dex lower, on average, than our Nançay detections. Some of these galaxies with low $M_{HI}/M_\star$ fractions lie in virtually unexplored parameter space (e.g., around $\log(L_r) = 11.5$) and could potentially be used to shed further light on galaxy evolution processes studied by modelers, e.g., Kannappan et al. (2013).

References

Benson, A. J., Bower, R. G., Frenk, C. S., et al. 2003, ApJ, 599, 38
Blanton, M. R., & Collaboration, S. 2001, AJ, 121, 2358
Blanton, M. R., Hogg, D. W., Brinkmann, J., et al. 2003, ApJ, 592, 819
Briggs, F., Sorar, E., Kraan-Korteweg, R., & Van Driel, W. 1997, PASA, 14, 37
Brinchmann, J., Charlot, S., White, S. D. M., et al. 2004, MNRAS, 351, 1151
de Vaucouleurs, G., de Vaucouleurs, A., Corwin, Jr., H. G., et al. 1991, Third Reference Catalogue of Bright Galaxies, Vol. I: Explanations and references, Vol. II: Data for galaxies between 0^h and 12^h, Vol. III: Data for galaxies between 12^h and 24^h (Springer-Verlag)
Efstathiou, G., Ellis, R. S., & Peterson, B. A. 1988, MNRAS, 232, 431
Felten, J. E. 1985, Comments on Astrophysics, 11, 53
Gavazzi, G., Fumagalli, M., Cucciati, O., & Boselli, A. 2010, A&A, 517, A73
Gehrels, N. 1986, ApJ, 303, 336
Giovanelli, R., Haynes, M. P., Kent, B. R., et al. 2005, AJ, 130, 2613
Haynes, M. P., Giovanelli, R., Martin, A. M., et al. 2011, AJ, 142, 170
Hoppmann, L., Staveley-Smith, L., Freudling, W., et al. 2015, MNRAS, 452, 3726
Huang, S., Haynes, M. P., Giovanelli, R., & Brinchmann, J. 2012, ApJ, 756, 113
Kannappan, S. J., Stark, D. V., Eckert, K. D., et al. 2013, ApJ, 777, 42
Kauffmann, G., Heckman, T. M., White, S. D. M., et al. 2003, MNRAS, 341, 33
Kilborn, V., Webster, R. L., & Staveley-Smith, L. 1999, PASA, 16, 8
Kovac, K., Oosterloo, T. A., & van der Hulst, J. M. 2005, Near-fields cosmology with dwarf elliptical galaxies, eds. H. Jerjen, & B. Binggeli, in IAU Colloq., 198, 351
Loveday, J., Peterson, B. A., Efstathiou, G., & Maddox, S. J. 1992, ApJ, 390, 338
Loveday, J., Norberg, P., Baldry, I. K., et al. 2015, MNRAS, 451, 1540
Lu, Y., Mo, H. J., Lu, Z., Katz, N., & Weinberg, M. D. 2014, MNRAS, 443, 1252
Martin, A. M., Papastergis, E., Giovanelli, R., et al. 2010, ApJ, 723, 1359
McNaught-Roberts, T., Norberg, P., Baugh, C., et al. 2014, MNRAS, 445, 2125
Montero-Dorta, A. D., & Prada, F. 2009, MNRAS, 399, 1106
Papastergis, E., Cattaneo, A., Huang, S., Giovanelli, R., & Haynes, M. P. 2012, ApJ, 759, 138
Saintonge, A. 2007, AJ, 133, 2087
Salim, S., Rich, R. M., Charlot, S., et al. 2007, ApJS, 173, 267
Schechter, P. 1976, ApJ, 203, 297
Schlegel, D. J., Finkbeiner, D. P., & Davis, M. 1998, ApJ, 500, 525
Schneider, S. E., Helou, G., Salpeter, E. E., & Terzian, Y. 1986, AJ, 92, 742
Schneider, S. E., Thuan, T. X., Magri, C., & Wadiak, J. E. 1990, ApJS, 72, 245
Springob, C. M., Haynes, M. P., & Giovanelli, R. 2005, ApJ, 621, 215
Tremonti, C. A., Heckman, T. M., Kauffmann, G., et al. 2004, ApJ, 613, 898
van Driel, W., Butcher, Z., Schneider, S., et al. 2016, A&A, 595, A118 (Paper I)
Wilson, T. L., Rohlfs, K., & Huttemeister, S. 2009, Tools of Radio Astronomy (Springer-Verlag)
York, D. G., Adelman, J., Anderson, Jr., J. E., et al. 2000, AJ, 120, 1579
Zwaan, M. A., Briggs, F. H., Sprayberry, D., & Sorar, E. 1997, ApJ, 490, 173
Zwaan, M. A., Staveley-Smith, L., Koribalski, B. S., et al. 2003, AJ, 125, 2842

Appendix A: Baseline derippling

Two of our sources, 1260 and 2434 (i.e., PGC 4546173 and CGCG 427-032), suffered from a baseline ripple with a wavelength of approximately 210 km s^{-1} due to reflected radiation in the telescope structure (see Briggs et al. 1997; Wilson et al. 2009). At Arecibo, this effect is caused by the formation of a standing wave between the primary mirror and receiver cabin. It can be caused by a number of phenomena but is typically the result of a strong continuum source or broadband terrestrial RFI. The ripple shows up in the spectrum as a result of a slight phase variation between the ON and OFF scans. In Fourier space, this manifests itself as a narrow spike corresponding to a period across 78 correlator channels or a wavelength of ~300 m (frequency of ~1 MHz). This is wavelength is exactly what one would expect to see in a standing wave since they form in multiples of half-wavelength distances between two reflecting surfaces. The distance between the primary mirror and the receiver cabin is 150 m.

To illustrate this phenomenon, in Fig. A.1a we show the spectrum of source 1260 as it originally appeared with the standing wave easily apparent, which we have over-layed in red for reference. The Fourier transform (Fig. A.1b) shows the effect of the ripple as two clearly identifiable spikes. After removing the offending period and doing an inverse Fourier transform (Fig. A.1c), the source signal is much more easily identified, resulting in a detection.
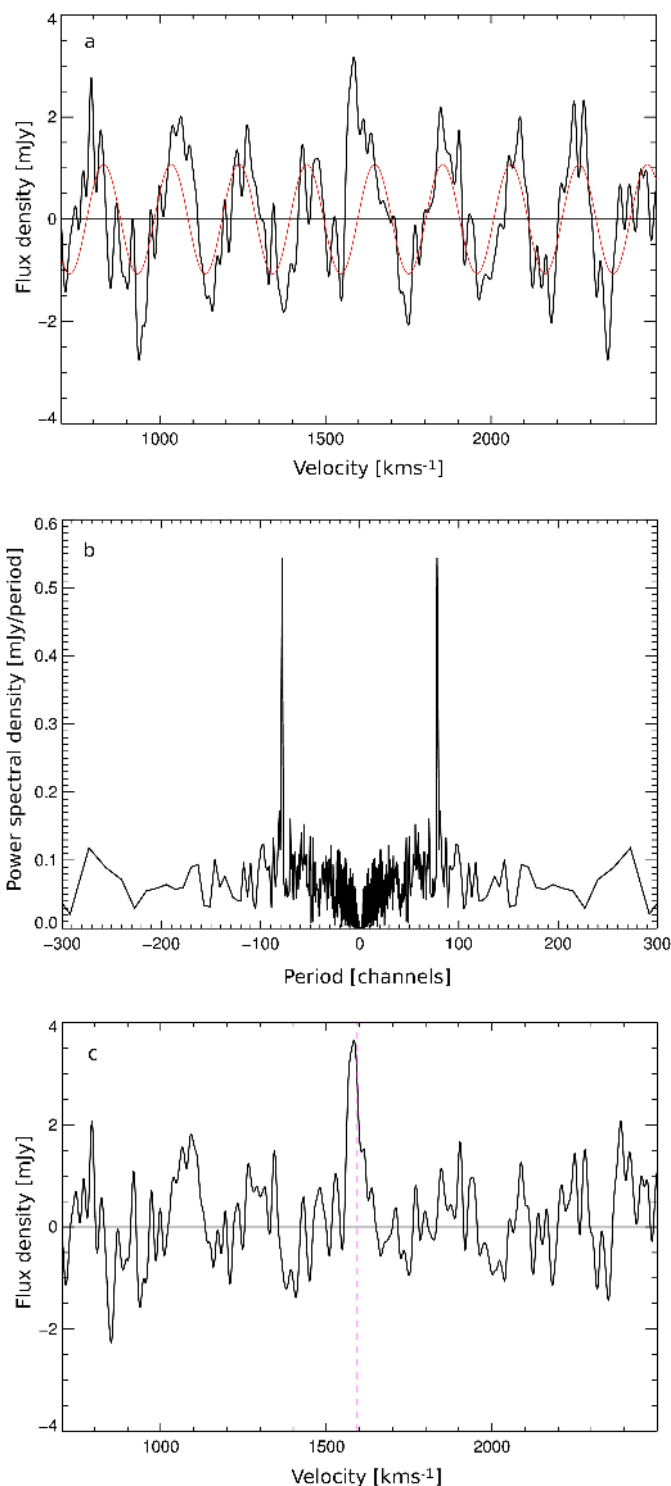
Fig. A.1. Illustration of the removal of a baseline ripple, in source 1260. **a)** Original observed H I line spectrum, flux density (mJy) as a function of heliocentric velocity with the standing wave over-layed in red. **b)** Spectral power density (mJy/period) vs. period for the Fourier transform where the spikes in power density corresponding to 78 channels due to the baseline ripple are clearly much higher than the rest of the spectrum. **c)** The reverse Fourier transform of **b)** with the 78 channel period peaks removed. The standing wave has clearly been eliminated from the spectrum and the source signal is now easily identified. The vertical magenta dashed line indicates the SDSS optical velocity. This illustration represents one of two cases in our sample where this procedure was used. Source 1260 contained the stronger of the two standing waves.
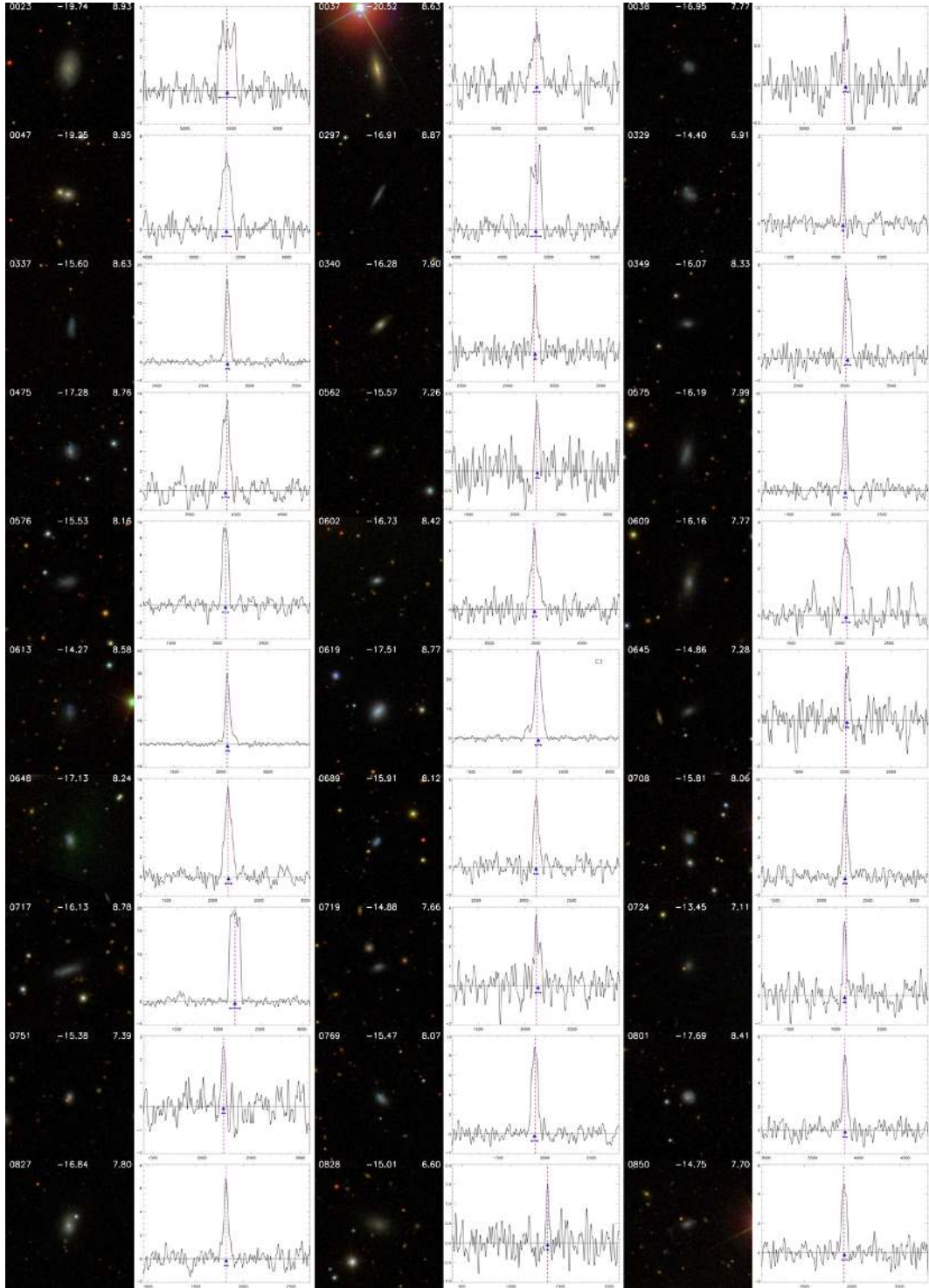
Appendix B: Arecibo spectra

Fig. B.1. Color (*g*, *r* and *i* band composite) images from the SDSS alongside 21-cm Hɪ line spectra of galaxies clearly detected at Arecibo. The size of each image is 2′ × 2′ with the NIBLES source number indicated in the *upper left corner*, absolute *z*-band magnitude, M_z, in the *top center* and log(M_{HI}) in $M_\odot$ in the *top right corner* of each image. The vertical axis in the spectra is flux density in mJy, the horizontal axis is heliocentric radial velocity (*cz*) in km s^{-1}. The SDSS recession velocity is denoted by a vertical dashed magenta line, the mean Hɪ velocity by the blue triangle, and the W_{50} line width by the horizontal blue arrow bar. Confused galaxies are denoted by their confusion code from Sect. 4 in the *upper right* portion of the spectrum. Velocity resolution is 18.7 km s^{-1}.
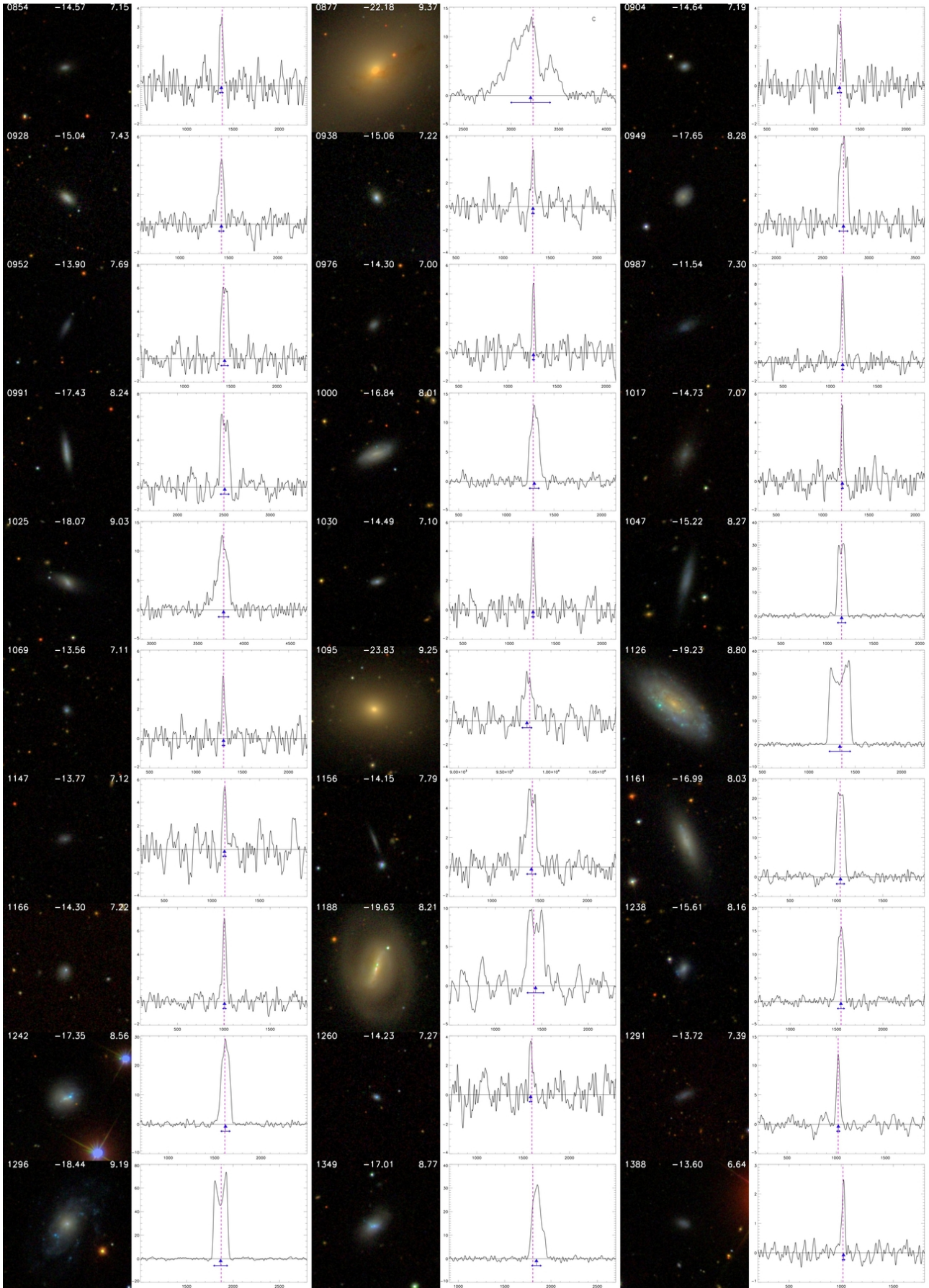
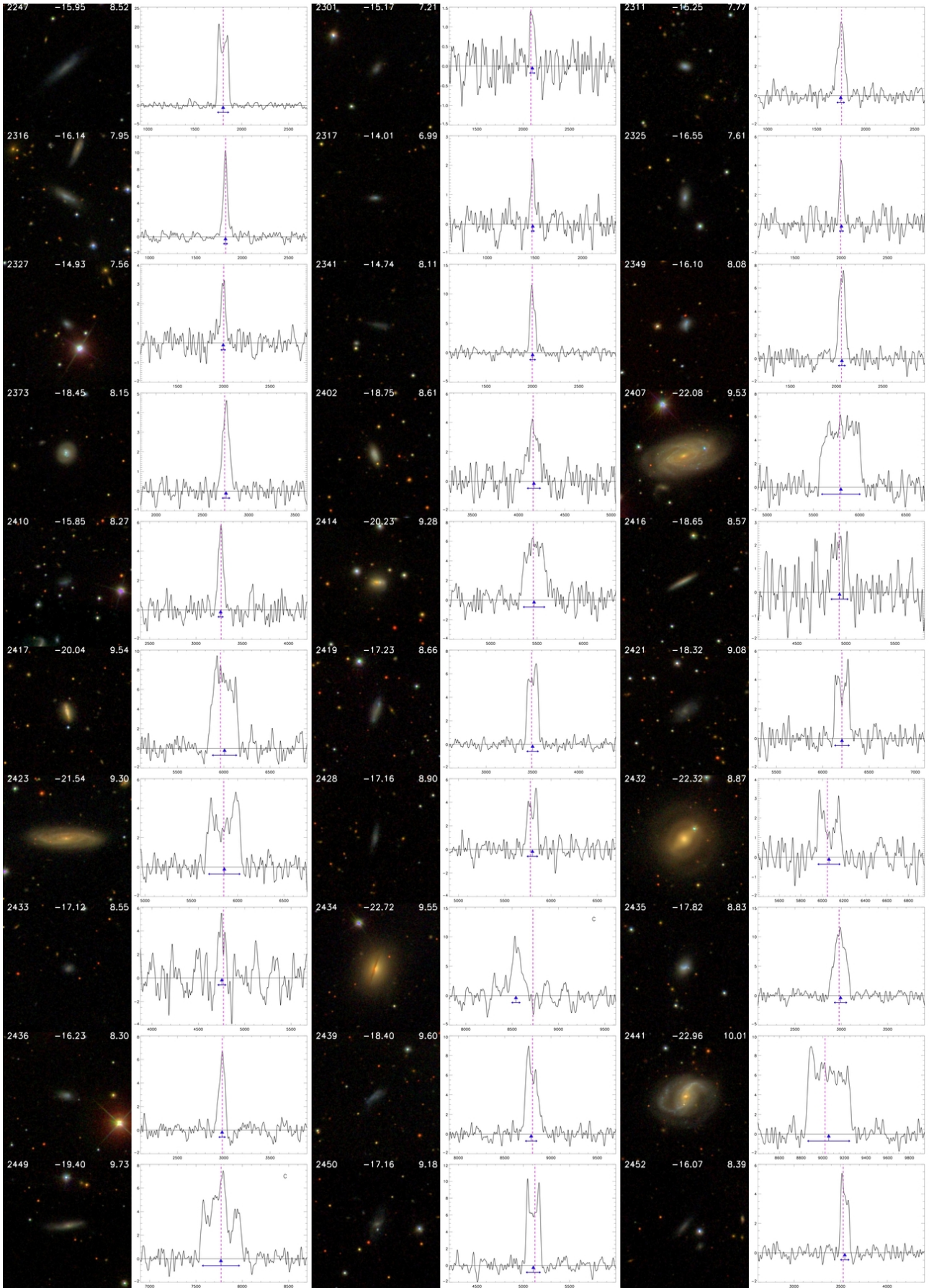**Fig. B.1.** continued.
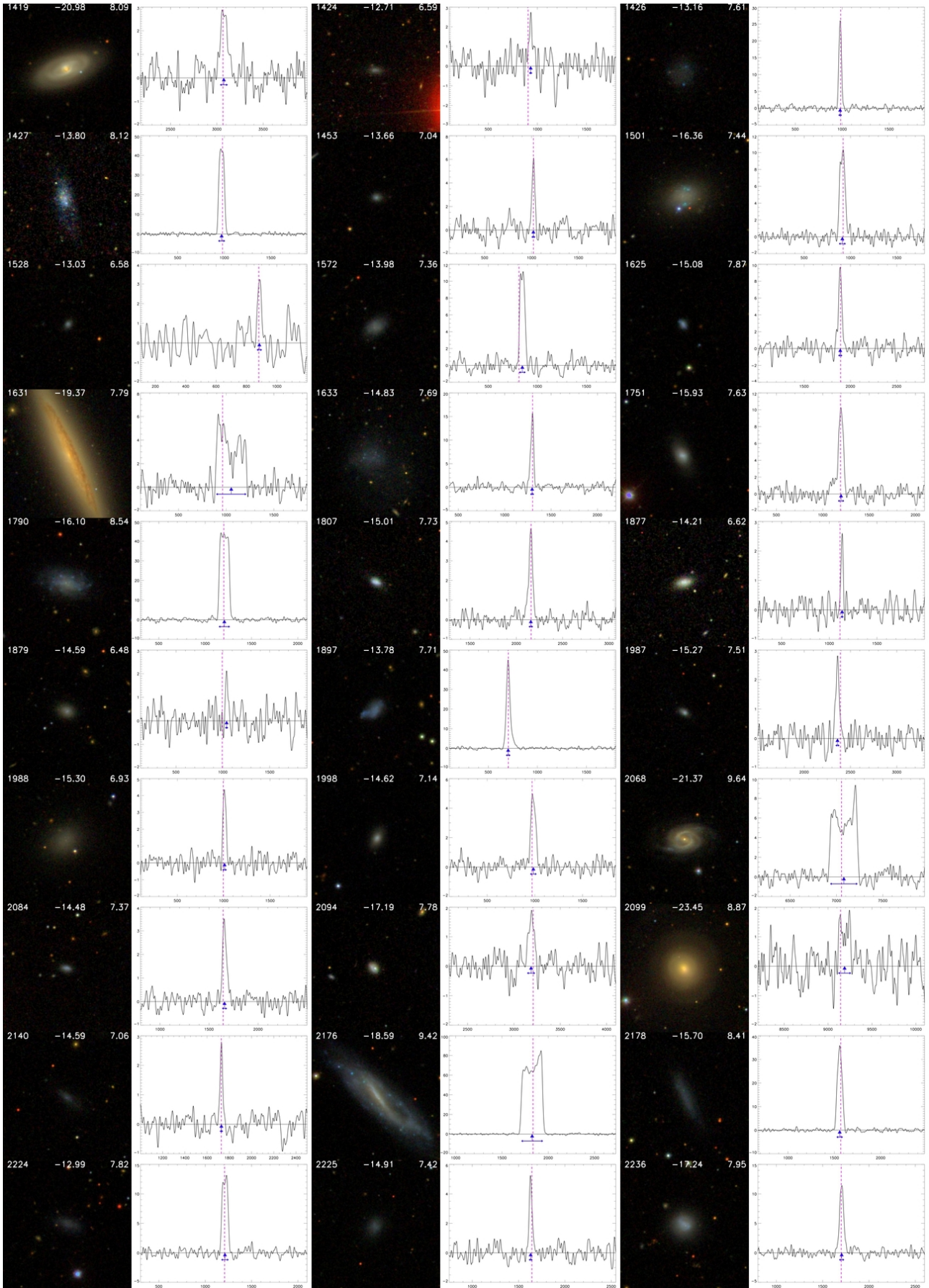
Fig. B.1. continued.
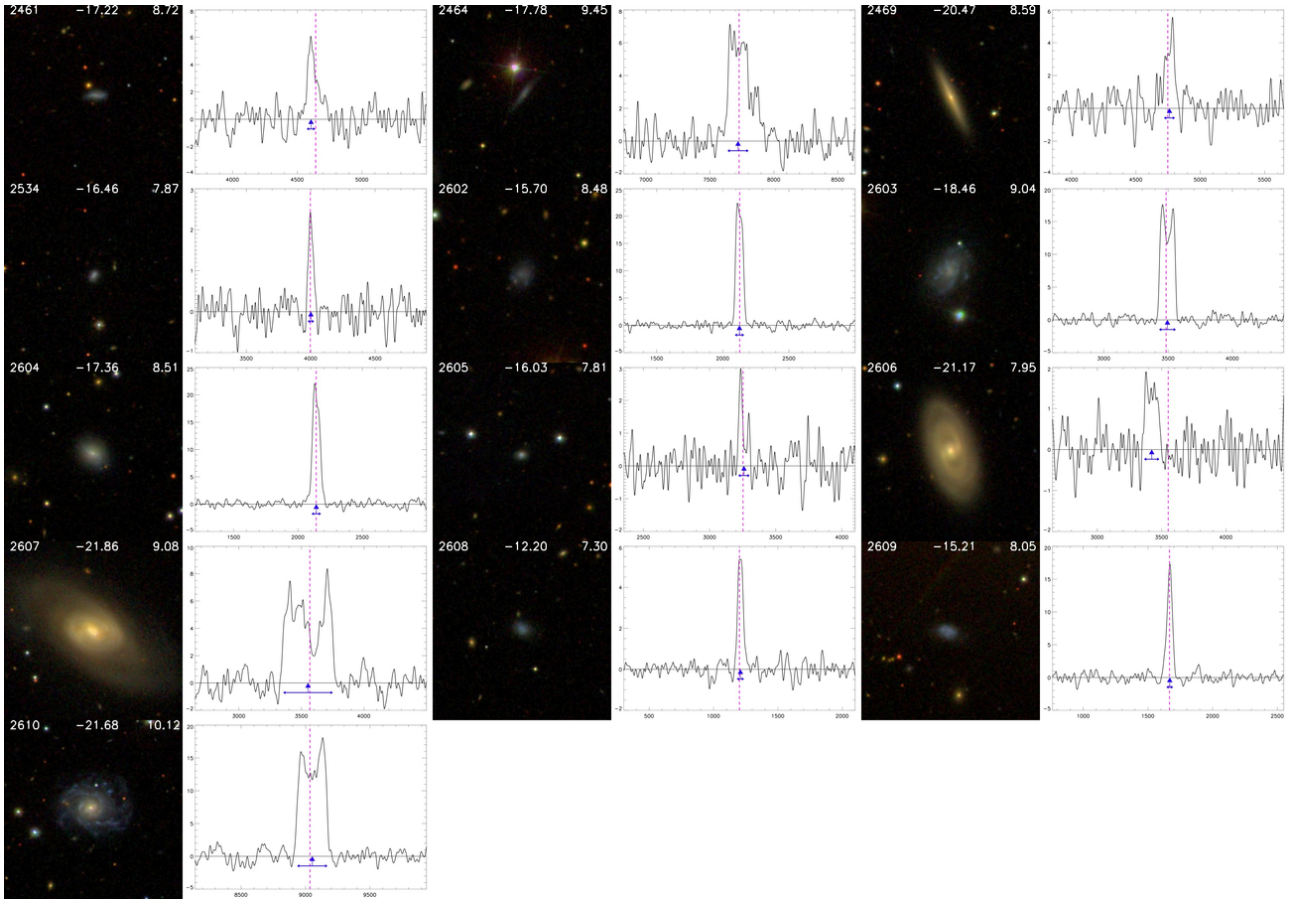
Fig. B.1. continued.
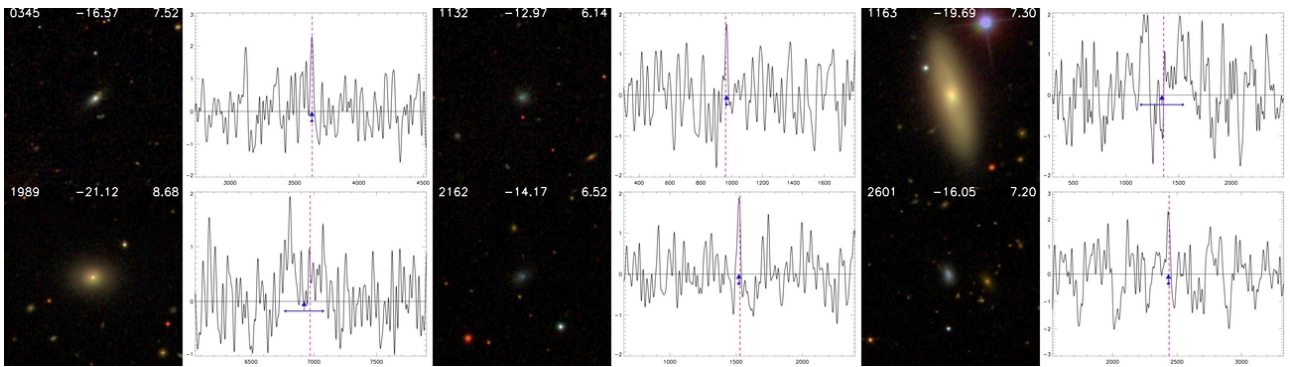
Fig. B.1. continued.

Fig. B.2. Color images from the SDSS alongside the 21-cm HI line spectra of galaxies marginally detected at Arecibo. See Fig. B.1 for further details.
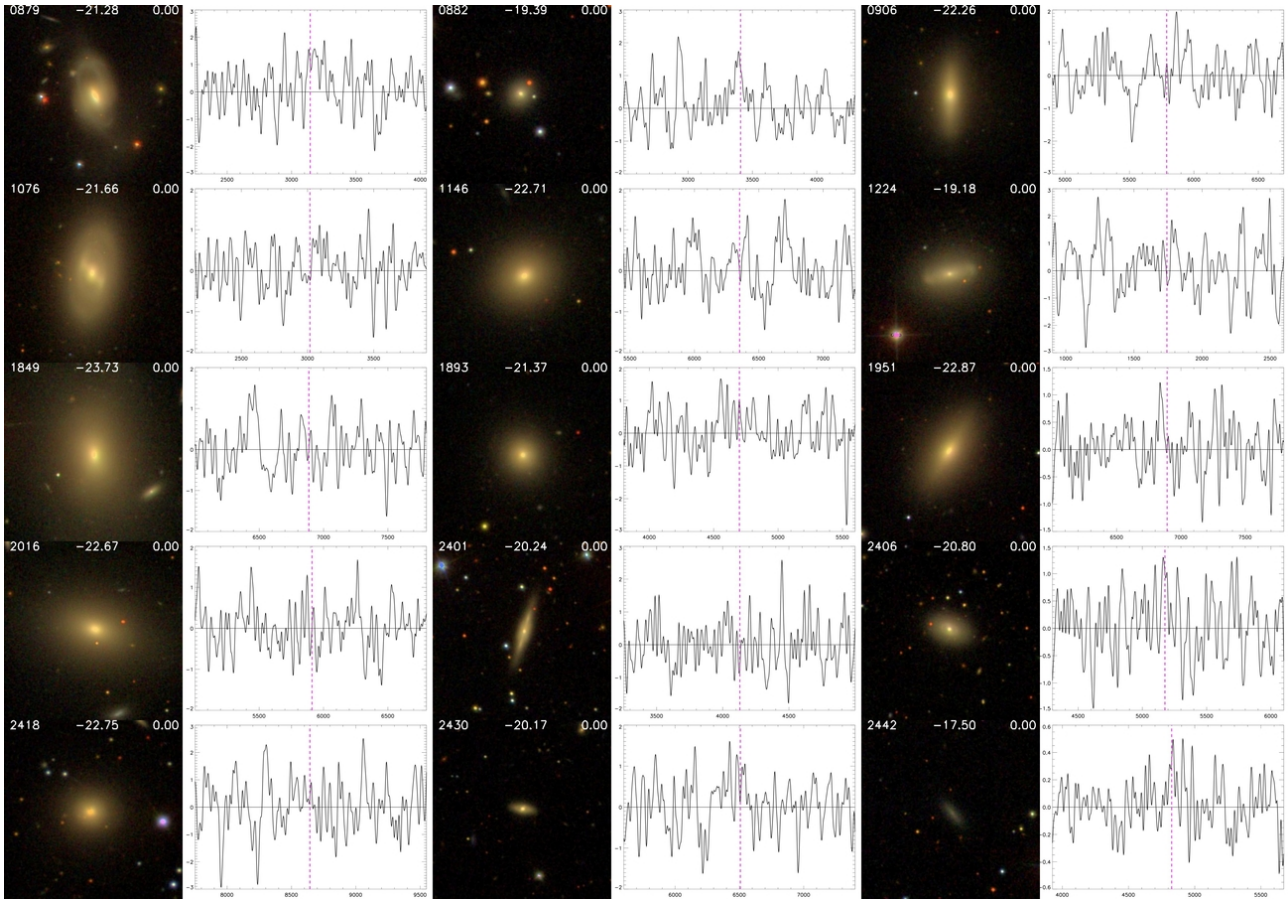
Fig. B.3. Color images from the SDSS alongside the 21-cm Hɪ line spectra of galaxies undetected at Arecibo. See Fig. B.1 for further details.